

Global sea-level rise in the early Holocene revealed from North Sea peats

Hijma, Marc P.; Bradley, Sarah L.; Cohen, Kim M.; van der Wal, Wouter; Barlow, Natasha L.M.; Blank, Bas; Frechen, Manfred; Hennekam, Rick; van Heteren, Sytze; More Authors

DOI

[10.1038/s41586-025-08769-7](https://doi.org/10.1038/s41586-025-08769-7)

Publication date

2025

Document Version

Final published version

Published in

Nature

Citation (APA)

Hijma, M. P., Bradley, S. L., Cohen, K. M., van der Wal, W., Barlow, N. L. M., Blank, B., Frechen, M., Hennekam, R., van Heteren, S., & More Authors (2025). Global sea-level rise in the early Holocene revealed from North Sea peats. *Nature*, 639(8055), 652-657. Article 106223. <https://doi.org/10.1038/s41586-025-08769-7>

Important note

To cite this publication, please use the final published version (if applicable). Please check the document version above.

Copyright

Other than for strictly personal use, it is not permitted to download, forward or distribute the text or part of it, without the consent of the author(s) and/or copyright holder(s), unless the work is under an open content license such as Creative Commons.

Takedown policy

Please contact us and provide details if you believe this document breaches copyrights. We will remove access to the work immediately and investigate your claim.

Global sea-level rise in the early Holocene revealed from North Sea peats

<https://doi.org/10.1038/s41586-025-08769-7>

Received: 25 April 2024

Accepted: 10 February 2025

Published online: 19 March 2025

Open access

 Check for updates

Marc P. Hijma^{1,2}✉, Sarah L. Bradley³, Kim M. Cohen⁴, Wouter van der Wal⁵, Natasha L. M. Barlow⁶, Bas Blank⁵, Manfred Frechen⁷, Rick Hennekam⁸, Sytze van Heteren⁹, Patrick Kiden⁹, Antonis Mavritsakos¹⁰, Bart M. L. Meijninger⁹, Gert-Jan Reichart^{8,11}, Lutz Reinhardt¹², Kenneth F. Rijdsdijk¹³, Annemiek Vink¹² & Freek S. Busschers⁹

Rates of relative sea-level rise during the final stage of the last deglaciation, the early Holocene, are key to understanding future ice melt and sea-level change under a warming climate¹. Data about these rates are scarce², and this limits insight into the relative contributions of the North American and Antarctic ice sheets to global sea-level rise during the early Holocene. Here we present an early Holocene sea-level curve based on 88 sea-level data points (13.7–6.2 thousand years ago (ka)) from the North Sea (Doggerland^{3,4}). After removing the pattern of regional glacial isostatic adjustment caused by the melting of the Eurasian Ice Sheet, the residual sea-level signal highlights two phases of accelerated sea-level rise. Meltwater sourced from the North American and Antarctic ice sheets drove these two phases, peaking around 10.3 ka and 8.3 ka with rates between 8 mm yr⁻¹ and 9 mm yr⁻¹. Our results also show that global mean sea-level rise between 11 ka and 3 ka amounted to 37.7 m (2σ range, 29.3–42.2 m), reconciling the mismatch that existed between estimates of global mean sea-level rise based on ice-sheet reconstructions and previously limited early Holocene sea-level data. With its broad spatiotemporal coverage, the North Sea dataset provides critical constraints on the patterns and rates of the late-stage deglaciation of the North American and Antarctic ice sheets, improving our understanding of the Earth-system response to climate change.

Rates of ice-sheet melt and associated sea-level rise (SLR) have been accelerating in response to global warming⁵. For the coming centuries, the Intergovernmental Panel on Climate Change⁵ expects that these rates will further increase to values not observed since the early Holocene¹ (11.7–8.2 thousand years ago (ka); all dates are in calibrated years BP). Accurate forecasting of future climate and sea level depends on a robust understanding of the Earth-system response to external forcings (for example, solar and orbital) and changes in atmospheric composition⁶. Although the available instrumental records provide detailed information about the functioning of our planet, Earth-system feedbacks on multi-centennial to millennial timescales cannot be evaluated using these short records. It is therefore necessary to obtain palaeorecords of sufficient detail, from periods like the early Holocene, that provide model benchmarks and climate storylines for present and near-future conditions.

During the early Holocene, temperatures increased rapidly⁷, resulting in large-scale melting of the remnant North American Ice Sheet Complex (NAISC, here Laurentide, Innuitian, Cordilleran and Greenland ice sheets combined) and sectors of the Antarctic Ice Sheet (AIS).

Early Holocene temporal changes in ice-sheet volume, as well as the modes through which meltwater reached the ocean (steadily or through pulses of proglacial lake-drainage events), have been reconstructed using empirical data^{8,9}, modelling results^{10,11} or combinations of both^{12,13}. Nevertheless, key uncertainties remain in terms of the timing of deglaciation and changes in ice-sheet volume. Patterns and rates of reconstructed relative sea level (RSL) are an important proxy for ice-sheet volume change and can therefore be used to calibrate and validate both ice-volume reconstructions¹⁴ and glacial isostatic adjustment (GIA) models^{10,14,15}. However, there are few geological constraints on early Holocene sea level, especially when compared with the middle and late Holocene, for which thousands of onshore collected sea-level index points (SLIPs) are available².

SLIPs are derived from dated indicators (for example, submerged peat layers, coral reefs and archaeological remains) that formed in close relationship with sea level and delimit the past position of sea level in space and time¹⁶. They are rare for the early Holocene, because records formed during that time typically occur offshore and are deeply buried, which makes them harder to sample. The limited early

¹Department of Subsurface Systems and Technologies, Deltares, Utrecht, The Netherlands. ²Department of Soil Geography and Landscape, Wageningen University and Research, Wageningen, The Netherlands. ³School of Geography and Planning, University of Sheffield, Sheffield, UK. ⁴Department of Physical Geography, Utrecht University, Utrecht, The Netherlands. ⁵Faculty of Aerospace Engineering, Delft University of Technology, Delft, The Netherlands. ⁶School of Earth and Environment, Leeds University, Leeds, UK. ⁷Department of Geochronology, LIAG Institute for Applied Geophysics, Hannover, Germany. ⁸Department of Ocean Systems, Royal Netherlands Institute for Sea Research (NIOZ), 't Horntje, The Netherlands. ⁹TNO – Geological Survey of the Netherlands, Utrecht, The Netherlands. ¹⁰Department of Safe and Resilient Infrastructure, Deltares, Delft, The Netherlands. ¹¹Department of Earth Sciences, Utrecht University, Utrecht, The Netherlands. ¹²Bundesanstalt für Geowissenschaften und Rohstoffe, Hannover, Germany. ¹³Institute for Biodiversity and Ecosystem Dynamics, University of Amsterdam, Amsterdam, The Netherlands. ✉e-mail: marc.hijma@deltares.nl

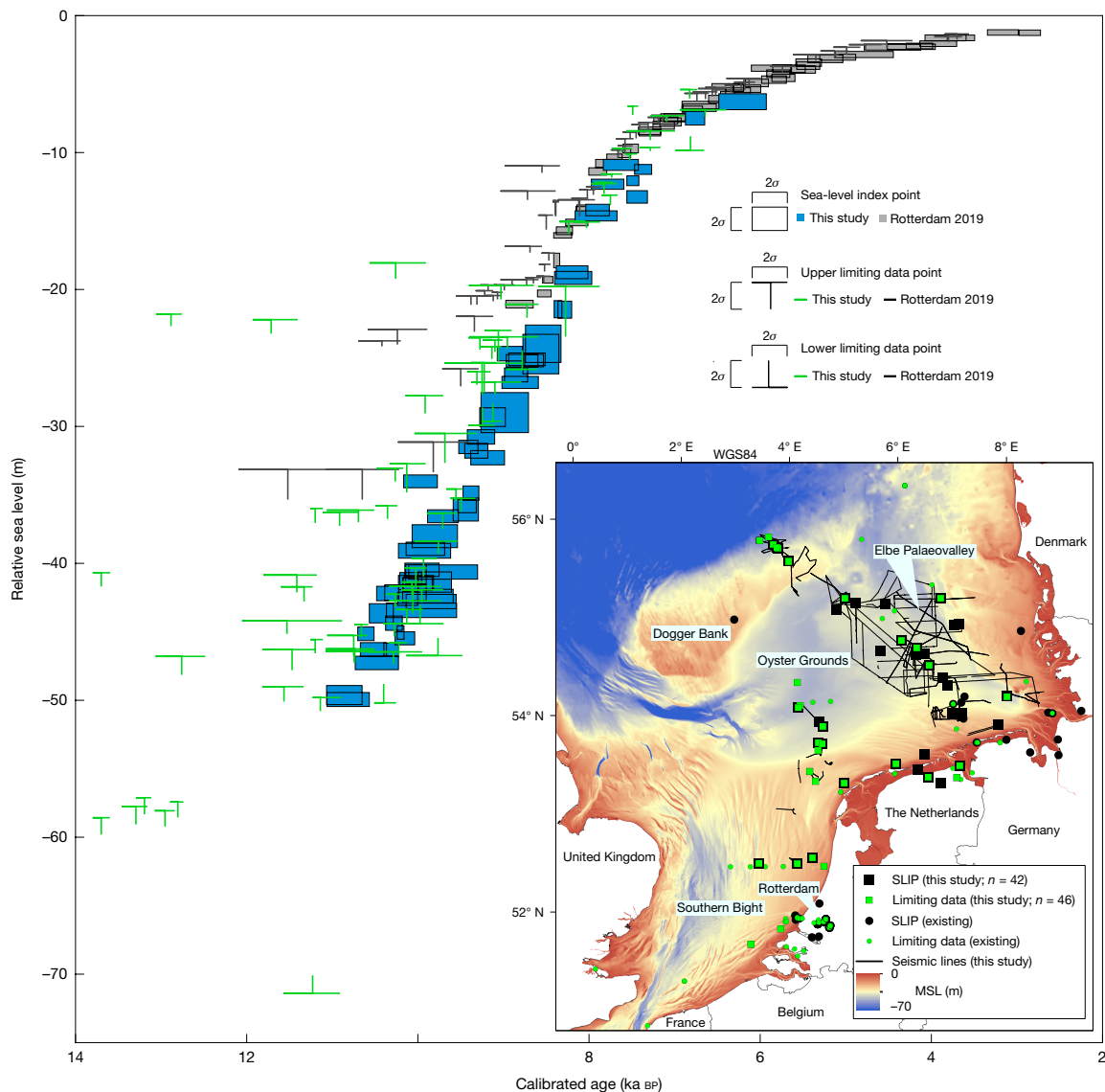


Fig. 1 | Plot of all SLIPs and limiting data points. The inset shows the locations of the data and the used seismic lines. Upper limiting data points provide an upper bound on the past position of the RSL and lower limiting data points provide a lower bound. The plotted RSL data points are corrected for

Holocene SLIP datasets that do exist have relatively large vertical uncertainties owing to: (1) low spatial sampling density (for example, isolated submerged mangrove peats¹⁷); (2) reliance on corals^{15,18,19} with relatively large depth–habitat ranges (often yielding 2σ uncertainties ≥ 8 m (ref. 20)); or (3) being substantially impacted by local ice loads²¹ (for example, rebound history). Where higher density and accuracy is reached, SLIP datasets do not extend before 9.5 ka (ref. 22). To fully employ the potential of using rates of SLR during the early Holocene to constrain rates of ice-volume change, regional SLIP series with high data density are required.

The North Sea region has an extensive shelf where such records are within reach of relatively low-cost shallow-depth sampling devices, with the advantage that temperate-latitude drowned-coastal marsh SLIPs sampled there have the potential for decimetre-scale precision¹⁶, although the region experiences proximal solid-earth responses to ice-loading patterns of the nearby Eurasian Ice Sheet (EuIS)^{23–25}. At the start of the Holocene, a large part of the North Sea was still dry land, over which widespread peat formation occurred before the archaeological ‘lost world’ of Doggerland^{3,4} was submerged in response to rising sea level. Despite subsequent erosion by coastal and marine processes,

compaction, palaeotidal variability and non-GIA background basin subsidence, but retain a spatially variable GIA signal. Bathymetric data in the inset were downloaded from EMODnet (<https://emodnet.ec.europa.eu/en/bathymetry>). WGS1984 is the World Geodetic System.

large stretches of these blanketing peats have been preserved^{25,26}. All previous sea-level studies in the North Sea region relied on relatively few legacy data points^{25,27} that are spatially isolated and show considerable discrepancies within and between subareas. These legacy data also have vertical uncertainties up to 4 m (2σ), which poorly constrain the early Holocene North Sea RSL and limit their usefulness in evaluating regional and global GIA modelling. As a result, the regional GIA contribution to modern SLR remains uncertain^{28,29}, complicating the translation of scenarios of future global SLR into regional predictions^{30,31}. Poorly constrained rates and magnitudes of RSL also mean that the magnitude, rate and timing of the contribution of late-stage deglaciation of the NAISC and the AIS to the global mean sea level (GMSL) remain uncertain. This is problematic as future SLR will be fuelled again from the melt of both the NAISC (primarily the Greenland Ice Sheet component) and the AIS. Hence, a comprehensive understanding of the complex interactions between climate, sea level and ice sheets during a rapidly warming global climate is required.

To better constrain rates of both the GMSL and the North Sea regional RSL, we obtained early Holocene SLIPs from the North Sea during multiple research cruises (Fig. 1). We applied GIA modelling to quantify the

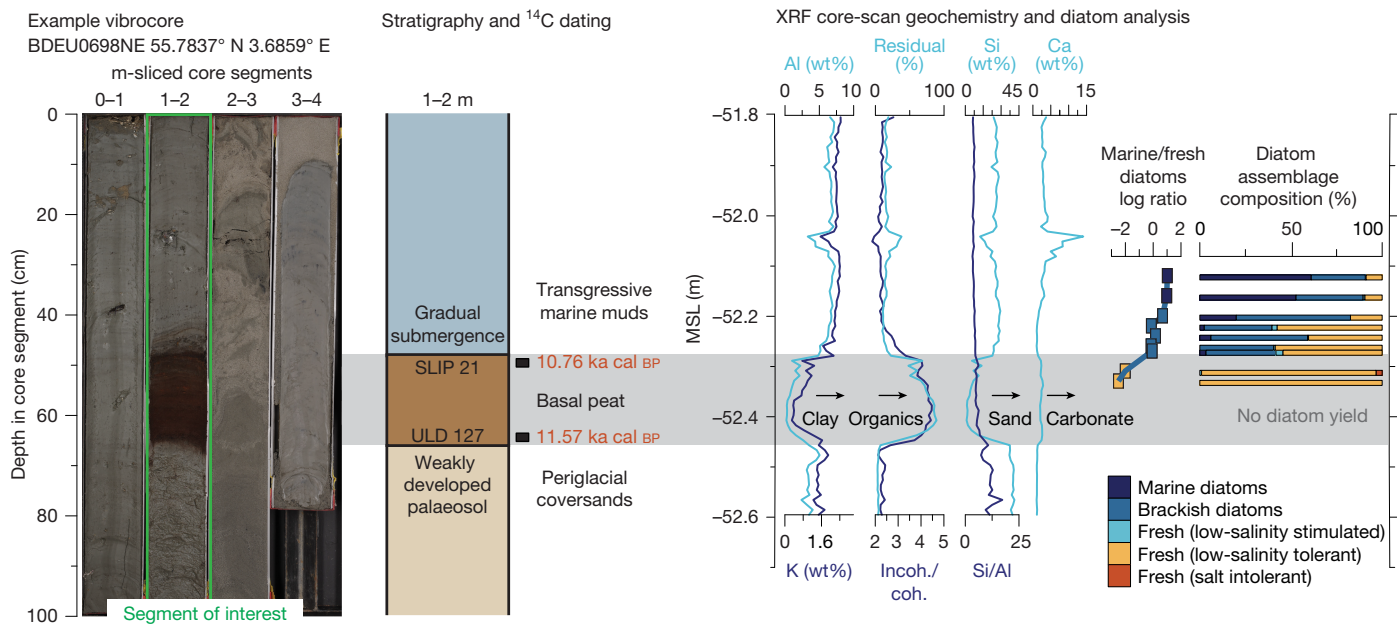


Fig. 2 | Example of a sampled sequence. The vibrocore reaches 3.8 m below the North Sea floor, with transgressed peat (basal peat) in photographed segment 1–2 m, and depth-aligned results for this segment representative of subsampling strategy and resolution of logging, dating, geochemical and palaeoenvironmental investigation to generate offshore sea-level data.

Figure collated from materials in supplementary information sections 1 (¹⁴C dating) and 2 (core photos, stratigraphic description, XRF core-scan results, diatom results; detailed single and multivariate geochemistry and diatom-species counts found in there)⁴⁹. BDEU0698NE = Core ID; SLIP, sea-level index point; ULD, upper limiting data point; cal, calibrated; Incoh./coh., Incoherent/coherent.

spatially varying contribution of the EuIS to the RSL in the North Sea. We then subtracted this EuIS contribution from each SLIP to isolate the combined contribution of the NAISC and the AIS to the GMSL (see Extended Data Fig. 1 for our workflow).

Sea-level data

The flooding of the North Sea is recorded in geological sequences that generally comprise a peat bed (0.1–0.3 m thick) overlying sandy Pleistocene deposits, and conformably underlying brackish marine muds^{25,32} (Fig. 2). Such transgressed-peat sequences formed extensively throughout the area during periods of early Holocene RSL rise, and the record of their drowning can be used to extract past sea-level positions. Erosion by subsequent shelf-sea dynamics led to a patchy preservation of in situ peat, typically buried by lags of shelly sands but locally by brackish muds. National borehole databases and geophysical data were used to target the collection of offshore vibrocores that contain the early Holocene peat–mud contact. We analysed diatom assemblages contained within the sediments and X-ray fluorescence (XRF) core-scan data to identify the palaeoenvironment recorded within the core and to assess whether the peat–mud contact is non-erosional.

Radiocarbon-dated samples from the bottom and mud-covered top of the peats constrain the age of the start and end of peat formation and provide details of the timing of transgression of the Holocene North Sea (Doggerland) landscape. We combined 88 sea-level data points with 51 legacy data points from the Dutch and German sectors of the North Sea. Legacy data from the British North Sea sector²¹ were not included, to avoid unwanted uncertainty caused by the regional British Ice Sheet load. The base of the peats yielded upper limiting data points (72 database entries; limiting data provide only upper or lower constraints on the elevation of past sea level), whereas the top of the peats yielded 59 SLIPs. Top-of-peat dates marking a boundary with freshwater lacustrine sediments, rather than brackish muds, are regarded as upper limiting data points (nine entries), and dates obtained from within brackish muds are regarded as lower limiting data points (eight entries). Vertical corrections were applied for compaction, palaeotidal

conditions³³ and non-GIA background basin subsidence, with propagation of associated uncertainties (Methods). We used Bayesian age modelling on clusters of radiocarbon dates to enforce stratigraphical order and RSL attribution³², thus reducing chronological uncertainties. The 59 North Sea SLIPs (of which 42 were recently gathered; Fig. 1) have a mean vertical uncertainty of ±0.42 m (2σ) and a mean age uncertainty of ±184 yr (2σ), both much smaller than in earlier studies^{15,25} that had uncertainties on the order of ±2 m (vertically) and ±500 yr (in time) for the early Holocene.

The SLIP dataset in this study shows that the North Sea RSL was around –50 m at 11 ka and rose to –15 m in the following 3 kyr. To improve our GIA modelling results and to extend our analysis into the Middle Holocene, we supplemented the offshore North Sea dataset with the nearby, mostly onshore, sea-level dataset³² for the Rotterdam area (50 SLIPs; Fig. 1).

Early Holocene SLR

The southern North Sea region shows large spatial variations in post-glacial RSL, reflecting a regional GIA pattern resulting from the deglaciation history of the proximal EuIS^{14,23,25} (Extended Data Figs. 6–8). To isolate the EuIS GIA component (including melt of its remaining ice sheet) contained in the Holocene RSL records from that driven by NAISC and AIS melt, we used two published EuIS reconstructions: ICE6G¹⁰ and BRITICE-CHRONO¹⁴, combined with a suite of one-dimensional (1D) and three-dimensional (3D) Earth models. From this suite, we selected eight models (seven 1D and one 3D; Extended Data Table 1) to calculate the EuIS RSL contribution for all SLIPs in Fig. 1. The 7 combinations with a 1D Earth model capture the RSL signal within a 95% confidence interval; the best-performing 3D model does not, but was included nonetheless to address any bias towards the assumption of a 1D rheology (Methods). The BRITICE-CHRONO-modelled EuIS contributions to RSL produced the lowest misfits when compared with the 109 SLIPs (Fig. 3; see Methods for details).

The best-fitting patterns with location-specific rates of EuIS GIA were subtracted from the SLIP observed RSL to generate a EuIS GIA-corrected

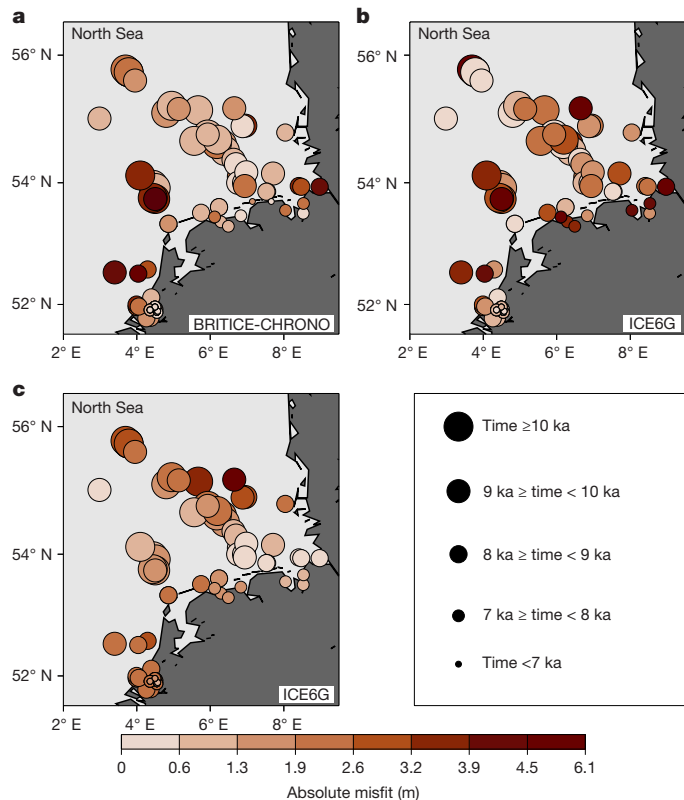


Fig. 3 | Absolute misfit between the SLIP-derived and modelled EuIS RSL signals. **a–c**, The BRITICE-CHRONO¹⁴ (**a**) and ICE6G¹⁰ (**b,c**) reconstructions are here combined with the 1D Earth model that produces the smallest misfit (**a,b**) and the largest misfit (**c**) (Extended Data Table 1). For BRITICE-CHRONO, this is a lithosphere thickness of 96 km combined with upper- and lower-mantle viscosities of 0.3×10^{21} Pa s and 20×10^{21} Pa s, respectively. For ICE6G, a lithosphere thickness of 96 km combined with upper- and lower-mantle viscosities of 0.5×10^{21} Pa s and 3×10^{21} Pa s, respectively (very similar to the VM5a Earth model, labelled ICE6G-smallest; **b**) and a lithosphere thickness of 71 km combined with upper- and lower-mantle viscosities of 0.5×10^{21} Pa s and 5×10^{21} Pa s, respectively (labelled ICE6G-largest; **c**).

sea-level dataset for the North Sea, with the standard deviation of the eight EuIS GIA-modelled predictions propagated in the uncertainty quantification. Thermosteric contributions (that is, the expansion of the ocean volume owing to temperature and salinity changes) during this time frame fluctuated around zero³⁴, whereas variations in the extent of mountain glaciers during the Holocene can be expected to result in decimetre-scale GMSL changes only^{35,36}. This means that after the EuIS contribution is removed from the RSL value of each SLIP, the resulting sea-level signal predominantly reflects the regional expression of the combined contribution of the North American and Antarctic ice sheets to early Holocene SLR. We label this signal ‘residual relative sea-level change’. The residual dataset was then processed with the Error-in-variables Integrated Gaussian Process (EIV-IGP) model^{37,38} that uses Bayesian inference to produce a continuous model (80-yr interval) of the rate of North Sea residual sea-level change (Fig. 4a). The high data density allows quantification of rates between 11 ka and 3 ka with a median uncertainty of ± 1.4 mm yr⁻¹ (2σ).

Phases of accelerated SLR

Our reconstruction of residual RSL for the North Sea shows two phases of accelerated SLR that span several centuries (Fig. 4a), which are attributed to phases of enhanced NAISC and AIS meltwater release. The first phase (P1) peaks around 10.3 ka, with a rate of nearly 9 mm yr⁻¹,

matching the maximum projected rates of GMSL rise for 2150 CE (Fig. 4a). Towards 9 ka, the rates drop to 5.7 mm yr⁻¹. The second phase (P2) peaks at 8.1 mm yr⁻¹ around 8.3 ka. Thereafter, rates decline rapidly to around 1 mm yr⁻¹ by 7.0 ka and to 0 mm yr⁻¹ by 5 ka. The negative rates between 5 ka and 3 ka are in line with evidence for regrowth of Antarctica during that time^{12,34}. The total North Sea residual sea-level change between 11 ka and 3 ka was 26.3 m (2σ range, 23.8–28.8 m; Fig. 4b).

In line with the timing of P2, several studies have identified the final, most likely two-staged drainage event³⁹ of Lake Agassiz–Ojibway, and related disintegration of sections of the NAISC, to be an important contributor to an accelerated phase of GMSL rise between 8.5 ka and 8.2 ka (refs. 32,40). This meltwater-release event explains a considerable part of P2 as Lake Agassiz–Ojibway alone contained an estimated 0.45 m sea-level equivalent (SLE)⁴¹. The remaining part of the SLR came from background melt of remnants of the Last Glacial ice sheets (with similar rates of SLR as at 9 ka)³². Without the storage of large quantities of meltwater in Lake Agassiz–Ojibway, the reconstructed dip in rates of SLR around 9 ka would have been smaller, and the peak in rates of SLR during P2 lower. It must be noted that during the drainage events, global rates of SLR were higher than 10 mm yr⁻¹ for relatively short periods of time^{32,40}.

By comparison, the timing, duration and magnitude of the rate of SLR during P1 has not been explained by any documented regionally sourced lake-drainage event. Recent work from the Labrador Sea, however, reports increased meltwater discharge between 10.64 ka and 10.15 ka (ref. 42), followed by a prolonged period of considerably lower meltwater discharge that increased again after 8.74 ka.

The large-scale meltwater-release signal observed between 11 ka and 8 ka from along the southern and eastern limits of NAISC⁴² thus aligns with the pattern found in the continuous, high-resolution record of the early Holocene residual RSL for the North Sea, with its vertical and temporal changes over multiple millennia. Herein, we consider P1 to be mainly a peak in ice-derived meltwater, directly linked to rapid climatic warming during the early Holocene. Several temperature records indicate that around 10 ka, global temperatures started to stabilize⁷, perhaps reflected in the timing of P1 termination. The warming would have set on at 11.7 ka (ref. 7), currently just out of reach of the North Sea SLIP data series. The rising limb of P1 as currently resolved (11–10.3 ka) consequently suffers from relatively large uncertainty that can be reduced only by obtaining additional SLIPs, for example, by sampling deeper lying and older peats from the North Sea. In contrast to P1, P2 has a more complex nature. It reflects a combination of the steady melt of ice sheets with the rapid release of water temporarily stored in large proglacial lakes and the associated rapid disintegration of parts of the Laurentide Ice Sheet.

GMSL and ice-sheet contributions

The North Sea residual RSL rise is the regional expression of early Holocene GMSL rise owing to steady loss of global land ice (Fig. 4b). The position of the North Sea with respect to the gravitational fingerprints of the Late Glacial and early Holocene ice sheets means that its early Holocene residual sea-level record captures 74% (2σ range, 68–90%) of GMSL (Methods and Extended Data Fig. 11). The 26.3 m (2σ range, 23.8–28.8 m; 74%; Fig. 4b) rise of North Sea residual RSL between 11 ka and 3 ka therefore translates to a global NAISC–AIS SLE of 35.5 m (2σ range, 27.1–40.0 m; 100%). Adding the EuIS contribution of 2.2 m SLE (2σ range, 1.5–2.9 m; see below) after 11 ka results in a total GMSL rise between 11 ka and 3 ka of 37.7 m (2σ range, 29.3–42.2 m). Far-field sea-level curves for the same period indicate a larger GMSL rise of 45 m to 55 m (refs. 15,19; with uncertainties estimated at ± 5 –10 m). This substantial mismatch is to be attributed in part to not accounting for spatially varying GIA-fingerprinting effects across widely scattered far-field shelf and island locations that can vary between 80% (ref. 43;

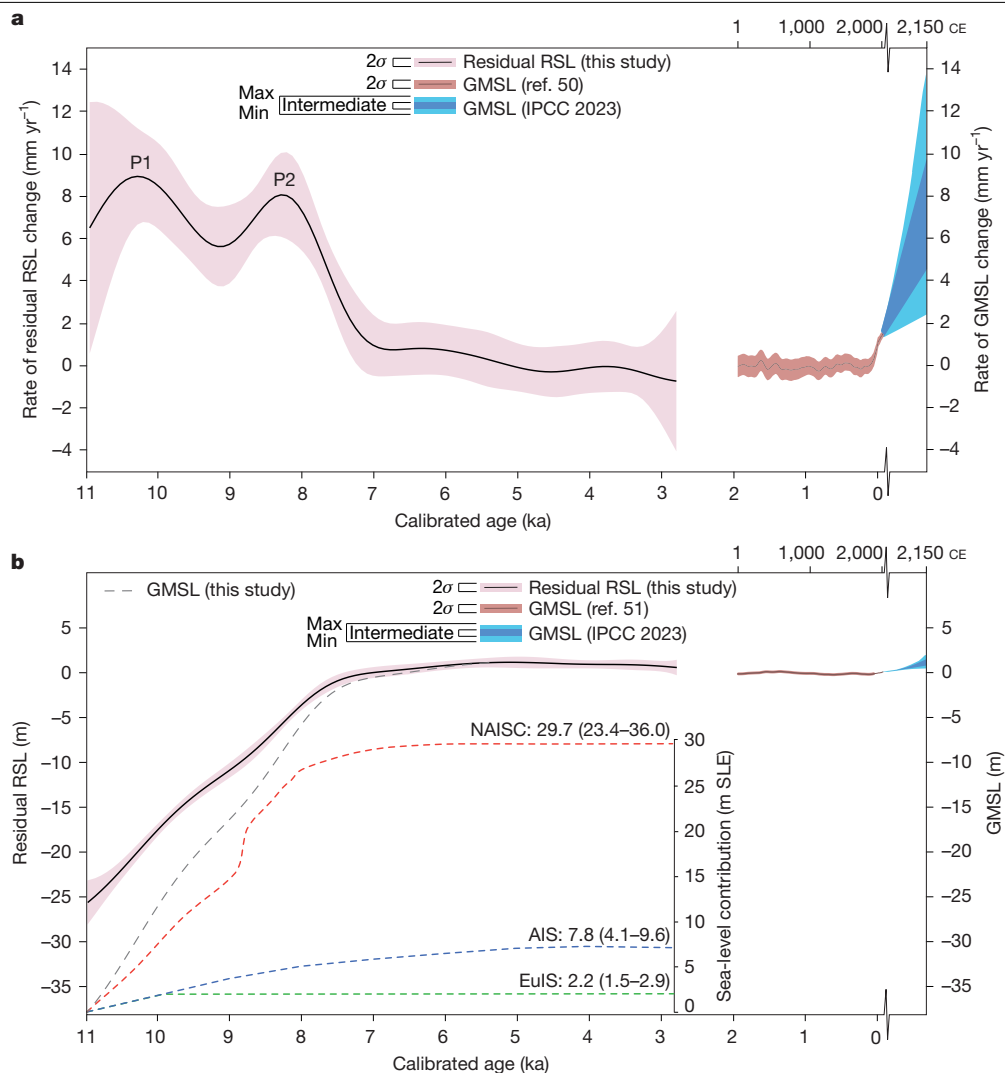


Fig. 4 | Rates and magnitude of early Holocene SLR. a, Rates of North Sea residual RSL change for 11–3 ka (data in⁴⁹), in relation to rates of GMSL change during the past 2 kyr (ref. 50) and expected for the next century⁵. **b**, North Sea residual RSL for 11–3 ka and the derived GMSL curve (dashed grey line) after accounting for regional NAISC–AIS sea-level fingerprint (this study). Also shown is GMSL during the past 2 kyr (ref. 51) and expected for the next

century⁵. The inset axis shows our reconstructed^{8,12,46–48} GMSL contributions in metres SLE from three main ice-mass centres (NAISC, AIS and EuIS) with their mean value and 2σ range. Data from 2 to 0 ka reproduced from: **a**, ref. 50, under a Creative Commons licence CC BY 4.0; **b**, ref. 51, under a Creative Commons licence CC BY 4.0.

for example, Barbados coral site) and 120% (ref. 43; for example, Tahiti coral site), and also to differing rates and modes of non-GIA subsidence/uplift between sites, and the complexities and associated large uncertainties when using coral as a sea-level indicator²⁰.

To evaluate the relative contribution of melt from the AIS, NAISC and EuIS to Holocene GMSL, we utilize published deglacial models and ice-sheet reconstructions. Constrained by geological data¹², recent deglacial simulations suggest that the AIS contributed 7.8 m SLE over the 11–3 ka period (2σ range, 4.1–9.6 m), in line with an earlier estimate⁴⁴. By contrast, another recent study estimated the AIS-derived contribution to GMSL over the same period as closer to 4 m SLE⁴⁵. Using geologically mapped ice-sheet extents⁸, our volumetric reconstructions of the NAISC over its deglaciation suggest that this ice-sheet complex contributed 29.7 m SLE (2σ range, 23.4–36.0 m) between 11 ka and 3 ka. The meltwater contribution of the EuIS over this period is much smaller, as its deglaciation was already nearly completed by the time the Holocene began: only 2.2 m SLE (2σ range, 1.5–2.9 m) after 11 ka (refs. 46–48).

Summing these respective ice-sheet contributions for 11–3 ka (Fig. 4b) results in a total GMSL rise of 39.7 m (2σ range, 32.3–46.3 m), in good agreement with the 37.7 m (2σ range, 29.3–42.2 m) of GMSL

rise we calculate based on the North Sea SLIPs. This reconciles the mismatch that existed between GMSL estimates based on ice-sheet reconstructions and previously limited and location-specific early Holocene sea-level data^{15,19}.

Our residual RSL record for the North Sea, which covers an area of approximately 80,000 km², highlights the importance of collecting densely sampled offshore RSL data with extensive overall spatial coverage. Such an approach offers improved constraints on ice-sheet reconstruction and GIA modelling for critical periods when ice sheets last melted as rapidly as anticipated in future GMSL projections. Specifically, it helps to constrain estimates of background GIA in both current regional RSL and projections of future SLR. Hence, we recommend (1) further early Holocene SLIP collection with similar spatial coverage and density as in the North Sea at selected shelf-sea sites worldwide, and (2) extension of data collection to the Late Glacial period, with North Sea seismic data showing accessible peat records to depths of about 80 m. Importantly, early Holocene sea-level data have an additional, direct application in geological, palaeoenvironmental and archaeological reconstructions of drowned shelf landscapes worldwide. By understanding the rapid RSL-driven flooding of these once-fertile lowlands

and important land bridges, these data records can shed light on one key driver of human migration in places such as Doggerland in north-west Europe^{3,4}. Dealing with climate change and rapid SLR is not unique to modern society.

Online content

Any methods, additional references, Nature Portfolio reporting summaries, source data, extended data, supplementary information, acknowledgements, peer review information; details of author contributions and competing interests; and statements of data and code availability are available at <https://doi.org/10.1038/s41586-025-08769-7>.

- Smith, D. E., Harrison, S., Firth, C. R. & Jordan, J. T. The early Holocene sea level rise. *Quat. Sci. Rev.* **30**, 1846–1860 (2011).
- Khan, N. S. et al. Inception of a global atlas of sea levels since the Last Glacial Maximum. *Quat. Sci. Rev.* **220**, 359–371 (2019).
- Cohen, K. M. & Hijma, M. P. in *Doggerland. Lost World under the North Sea* (eds Amkreutz, L. W. S. W. & Van der Vaart-Verschoof, S.) 31–35 (Sidestone Press, 2022).
- Gaffney, V., Fitch, S. & Smith, D. *Europe's Lost World: the Rediscovery of Doggerland* (Council for British Archeology, 2009).
- Fox-Kemper, B. et al. in *Climate Change 2021: The Physical Science Basis* (eds Masson-Delmotte, V. et al.) 1211–1362 (IPCC, Cambridge Univ. Press, 2023).
- Masson-Delmotte, V. et al. in *Climate Change 2013: The Physical Science Basis* (eds Stocker, T. F. et al.) 383–464 (IPCC, Cambridge Univ. Press, 2013).
- Kaufman, D. S. & Broadman, E. Revisiting the Holocene global temperature conundrum. *Nature* **614**, 425–435 (2023).
- Dalton, A. S. et al. An updated radiocarbon-based ice margin chronology for the last deglaciation of the North American Ice Sheet Complex. *Quat. Sci. Rev.* **234**, 106223 (2020).
- Bentley, M. J. et al. A community-based geological reconstruction of Antarctic Ice Sheet deglaciation since the Last Glacial Maximum. *Quat. Sci. Rev.* **100**, 1–9 (2014).
- Peltier, W. R., Argus, D. F. & Drummond, R. Space geodesy constrains ice age terminal deglaciation: the global ICE-6G_C (VM5a) model. *J. Geophys. Res. Solid Earth* **120**, 450–487 (2015).
- Ullman, D. J., Carlson, A. E., Anslow, F. S., LeGrande, A. N. & Licciardi, J. M. Laurentide ice-sheet instability during the last deglaciation. *Nat. Geosci.* **8**, 534–537 (2015).
- Pittard, M. L., Whitehouse, P. L., Bentley, M. J. & Small, D. An ensemble of Antarctic deglacial simulations constrained by geological observations. *Quat. Sci. Rev.* **298**, 107800 (2022).
- Carlson, A. E. & Clark, P. U. Ice sheet sources of sea level rise and freshwater discharge during the last deglaciation. *Rev. Geophys.* <https://doi.org/10.1029/2011RG000371> (2012).
- Bradley, S. L., Ely, J. C., Clark, C. D., Edwards, R. J. & Shennan, I. Reconstruction of the palaeo-sea level of Britain and Ireland arising from empirical constraints of ice extent: implications for regional sea level forecasts and North American ice sheet volume. *J. Quat. Sci.* **38**, 791–805 (2023).
- Lambeck, K., Rouby, H., Purcell, A., Sun, Y. & Sambridge, M. Sea level and global ice volumes from the Last Glacial Maximum to the Holocene. *Proc. Natl Acad. Sci. USA* **111**, 15296–15303 (2014).
- Shennan, I., Long, A. J. & Horton, B. P. (eds) *Handbook of Sea-Level Research* (Wiley/AGU, 2015).
- Hanebuth, T., Stattegger, K. & Grootes, P. M. Rapid flooding of the Sunda Shelf: a late-glacial sea-level record. *Science* **288**, 1033–1035 (2000).
- Khan, N. S. et al. Drivers of Holocene sea-level change in the Caribbean. *Quat. Sci. Rev.* **155**, 13–36 (2017).
- Bard, E., Hamelin, B. & Delanghe-Sabatier, D. Deglacial meltwater pulse 1B and Younger Dryas sea levels revisited with boreholes at Tahiti. *Science* **327**, 1235–1237 (2010).
- Hibbert, F. D. et al. Coral indicators of past sea-level change: a global repository of U-series dated benchmarks. *Quat. Sci. Rev.* **145**, 1–56 (2016).
- Shennan, I., Bradley, S. L. & Edwards, R. Relative sea-level changes and crustal movements in Britain and Ireland since the Last Glacial Maximum. *Quat. Sci. Rev.* **188**, 143–159 (2018).
- Chua, S. et al. A new Holocene sea-level record for Singapore. *Holocene* **31**, 1376–1390 (2021).
- Kiden, P., Denys, L. & Johnston, P. Late Quaternary sea-level change and isostatic and tectonic land movement along the Belgian–Dutch North Sea coast: geological data and model results. *J. Quat. Sci.* **17**, 535–546 (2002).
- Steffen, H. & Wu, P. Glacial isostatic adjustment in Fennoscandia—a review of data and modeling. *J. Geodyn.* **52**, 169–204 (2011).
- Vink, A., Steffen, H., Reinhardt, L. & Kaufmann, G. Holocene relative sea-level change, isostatic subsidence and the radial viscosity structure of the mantle of northwest Europe (Belgium, the Netherlands, Germany, southern North Sea). *Quat. Sci. Rev.* **26**, 3249–3275 (2007).
- Eaton, S., Barlow, N. L. M., Hodgson, D. M., Mellett, C. L. & Emery, A. R. Landscape evolution during Holocene transgression of a mid-latitude low-relief coastal plain: the southern North Sea. *Earth Surf. Process. Landf.* **49**, 3139–3157 (2024).
- Shennan, I. et al. Modelling western North Sea palaeogeographies and tidal changes during the Holocene. *Geol. Soc. Lond. Spec. Publ.* **166**, 299–319 (2000).
- Love, R. et al. The contribution of glacial isostatic adjustment to projections of sea-level change along the Atlantic and Gulf coasts of North America. *Earths Future* **4**, 440–464 (2016).
- Spada, G. & Melini, D. New estimates of ongoing sea level change and land movements caused by glacial isostatic adjustment in the Mediterranean region. *Geophys. J. Int.* **229**, 984–998 (2021).
- Vermeersen, B. L. A. et al. Sea-level change in the Dutch Wadden Sea. *Neth. J. Geosci.* **97**, 79–127 (2018).
- Van de Wal, R. S. W. et al. A high-end estimate of sea level rise for practitioners. *Earths Future* **10**, e2022EF002751 (2022).
- Hijma, M. P. & Cohen, K. M. Holocene sea-level database for the Rhine-Meuse Delta, The Netherlands: implications for the pre-8.2 ka sea-level jump. *Quat. Sci. Rev.* **214**, 68–86 (2019).
- Ward, S. L., Neill, S. P., Scourse, J. D., Bradley, S. L. & Uehara, K. Sensitivity of palaeotidal models of the northwest European shelf seas to glacial isostatic adjustment since the Last Glacial Maximum. *Quat. Sci. Rev.* **151**, 198–211 (2016).
- Creel, R. C. et al. Global mean sea level likely higher than present during the holocene. *Nat. Commun.* <https://doi.org/10.1038/s41467-024-54535-0> (2024).
- Solomina, O. N. et al. Holocene glacier fluctuations. *Quat. Sci. Rev.* **111**, 9–34 (2015).
- Gangadharan, N. et al. Process-based estimate of global-mean sea-level changes in the Common Era. *Earth Syst. Dyn.* **13**, 1417–1435 (2022).
- Cahill, N., Kemp, A. C., Horton, B. P. & Parnell, A. C. A Bayesian hierarchical model for reconstructing relative sea level: from raw data to rates of change. *Clim. Past* **12**, 525–542 (2016).
- Cahill, N., Kemp, A. C., Horton, B. P. & Parnell, A. C. Modeling sea-level change using errors-in-variables integrated Gaussian processes. *Ann. Appl. Stat.* **9**, 547–571 (2015).
- Brouard, E., Roy, M., Godbout, P.-M. & Veillette, J. J. A framework for the timing of the final meltwater outbursts from glacial Lake Agassiz–Ojibway. *Quat. Sci. Rev.* **274**, 107269 (2021).
- Rush, G. et al. The magnitude and source of meltwater forcing of the 8.2 ka climate event constrained by relative sea-level data from eastern Scotland. *Quat. Sci. Adv.* **12**, 100119 (2023).
- Leverington, D. W., Mann, J. D. & Teller, J. T. Changes in the bathymetry and volume of glacial Lake Agassiz between 9,200 and 7,700 ¹⁴C yr BP. *Quat. Res.* **57**, 244–252 (2002).
- You, D. et al. Last deglacial abrupt climate changes caused by meltwater pulses in the Labrador Sea. *Commun. Earth Environ.* **4**, 81 (2023).
- Lin, Y. et al. A reconciled solution of meltwater pulse 1A sources using sea-level fingerprinting. *Nat. Commun.* **12**, 2015 (2021).
- Mackintosh, A. et al. Retreat of the East Antarctic ice sheet during the last glacial termination. *Nat. Geosci.* **4**, 195–202 (2011).
- Golledge, N. R. et al. Retreat of the Antarctic Ice Sheet during the last interglaciation and implications for future change. *Geophys. Res. Lett.* **48**, e2021GL094513 (2021).
- Hughes, A. L. C., Gyllencreutz, R., Lohne, Ø. S., Mangerud, J. & Svendsen, J. I. The last Eurasian ice sheets—a chronological database and time-slice reconstruction, DATED-1. *Boreas* **45**, 1–45 (2016).
- Patton, H. et al. Deglaciation of the Eurasian ice sheet complex. *Quat. Sci. Rev.* **169**, 148–172 (2017).
- Cuzzone, J. K. et al. Final deglaciation of the Scandinavian Ice Sheet and implications for the Holocene global sea-level budget. *Earth Planet. Sci. Lett.* **448**, 34–41 (2016).
- Hijma, M. P. et al. Global sea-level rise in the early Holocene revealed from North Sea peats: supplementary information. *Zenodo* <https://doi.org/10.5281/zenodo.10801302> (2025).
- Walker, J. S., Kopp, R. E., Little, C. M. & Horton, B. P. Timing of emergence of modern rates of sea-level rise by 1863. *Nat. Commun.* **13**, 966 (2022).
- Walker, J. S. et al. Common Era sea-level budgets along the U.S. Atlantic coast. *Nat. Commun.* **12**, 1841 (2021).

Publisher's note Springer Nature remains neutral with regard to jurisdictional claims in published maps and institutional affiliations.



Open Access This article is licensed under a Creative Commons Attribution-NonCommercial-NoDerivatives 4.0 International License, which permits any non-commercial use, sharing, distribution and reproduction in any medium or format, as long as you give appropriate credit to the original author(s) and the source, provide a link to the Creative Commons licence, and indicate if you modified the licensed material. You do not have permission under this licence to share adapted material derived from this article or parts of it. The images or other third party material in this article are included in the article's Creative Commons licence, unless indicated otherwise in a credit line to the material. If material is not included in the article's Creative Commons licence and your intended use is not permitted by statutory regulation or exceeds the permitted use, you will need to obtain permission directly from the copyright holder. To view a copy of this licence, visit <http://creativecommons.org/licenses/by-nc-nd/4.0/>.

© The Author(s) 2025

Methods

Before detailing each step in our methodology in the following sections, we first explain the main rationale behind our approach to distil a GMSL curve from our North Sea sea-level dataset for the 11–3 ka period. The dataset is used to construct SLIPs (steps 1 and 2 in Extended Data Fig. 1) that show strong spatial variation in RSL histories owing to the proximal location of the North Sea region to the EuS and the resulting non-uniform EuS GIA signal. This signal consists mostly of a vertical-land-motion component, because EuS volume loss constitutes only 2.2 m SLE (2σ range, 1.5–2.9 m) after 11 ka (refs. 46–48). To isolate the much larger Holocene ice-sheet volume loss from the NAISC and the AIS, we subtracted the predicted EuS GIA signal from the observed SLIP value. The resulting sea-level signal is labelled ‘residual relative sea-level change’.

The predicted EuS GIA signal was calculated by running a large array of GIA models (both 1D and 3D) and selecting the best-performing models (seven 1D models and one 3D model; step 3). For performance testing of the GIA models, we included the existing, adjacent Rotterdam sea-level dataset that was gathered mostly onshore and has the same high level of spatial and temporal resolution³². The residual RSL record (step 4) is of smaller vertical range and spatially much more uniform than the RSL record produced in step 2. The residual RSL record therefore is considered a regional expression of the contribution of meltwater coming from the NAISC and the AIS to early Holocene SLR. We prefer this approach of obtaining a residual RSL record over simply using the eight selected GIA models directly to calculate the NAISC and AIS contributions in the early Holocene, as this would neglect the independent and observational value of the geological sea-level data and mainly mimic the NAISC and AIS reconstructions that were used in the GIA model itself.

In step 5, we used the residual sea-level data to construct a North Sea residual RSL curve for 11–3 ka and calculate rates of SLR with the Bayesian EIV-IPG model^{37,38}. In step 6, we determined a sea-level fingerprint correction factor specific to the region and early Holocene time frame and used it to convert the North Sea residual RSL curve to a GMSL curve for 11–3 ka.

Our sea-level data (steps 1 and 2)

National borehole databases^{52,53} guided the identification of offshore locations with good prospects of preserved peat sequences within maximum target depths reachable by vibrocoreing. During research cruises in 2009⁵⁴, 2011⁵⁵, 2017⁵⁶ and 2018, geophysical surveys were undertaken using sub-bottom profilers, boomers and sparkers to map the distribution and depth of the peat along 4,400-line km, used to determine exact core locations. Up to 6-m-long vibrocores were then retrieved, cut in metre-long sections, stored at 4 °C, transported to land, split lengthwise, and sedimentologically and stratigraphically logged (for all cruises). Vibrocores for the 2017–2018 cruises were also XRF-scanned (Extended Data Fig. 1, step 1).

Tops and bases of compacted peat beds resting on consolidated substrates were subsampled for the identification and selection of macrofossils for accelerator mass spectrometry radiocarbon dating (Fig. 2; see also supplementary information section 1 (supplementary information is available on Zenodo at <https://doi.org/10.5281/zenodo.10801302> (ref. 49)). From several cores, diatom assemblages were identified (Fig. 2). The combined information was used to produce a database of RSL data points (Fig. 1) following the HOLSEA protocol^{2,32} (Extended Data Fig. 1, step 2). Additional data fields were included to specify (1) a series of vertical correction terms (decompaction, palaeotidal variability, background basin subsidence), (2) the Bayesian radiocarbon age calibration⁵⁷, and (3) the labelling as SLIP, upper limiting (sometimes called terrestrial in literature) or lower limiting data point, or rejected point. Legacy data were also entered into the database and were re-analysed with the same protocol. Supplementary

information section 1 contains the full database, including technical documentation for contents and calculation of each field and supplementary information section 2 contains the analyses of the XRF and diatom data, as well as core photos⁴⁹.

Extended Data Fig. 2 presents a sensitivity analysis (Extended Data Fig. 1, step 5) of the impact of each correction term on the calculated rates of MSL rise. It shows a relative insensitivity to the applied compaction correction (decompaction factor of 3 ± 0.5 based on modelled bulk density⁵⁸), because the majority of the SLIP-providing peat beds were <0.3 m thick. Rates are more sensitive to the incorporation of palaeotidal information^{33,59–61} (literature-obtained amplitudes $\pm 37.5\%$ uncertainty³²; supplementary information⁴⁹ section 1) when converting from mean high water (the reference water level for SLIPs from drowned peats in this area^{62,63}) to MSL. The correction for background basin subsidence (that is, non-GIA vertical land motion) is most impactful, albeit spatially variable, with maximum upwards corrections of 2.7–2.9 m for 11-ka-old SLIPs from the subsidence centre (Extended Data Fig. 3). In our specification of background basin subsidence across the study area, we made use of a recently compiled data product considering the geologically mapped thickness of North Sea Basin fill for two periods: postdating 2.6 million years ago (Ma; regionally mapped; ‘base Quaternary’) versus postdating 1.8 Ma (subregionally known; ‘base Olduvai’) (supplementary information⁴⁹ section 3; combining onshore and offshore data products of Dutch and German geological surveys; also used in the analysis of a recent Last Interglacial sea-level database⁶⁴).

Bulk sediment (2009–2011 cruises) or selected macrofossils (2017–2018 cruises) from thin (mostly 0.02 m thick) slices of the top and bottom of the peat were submitted for accelerator mass spectrometry ¹⁴C dating. Bayesian age calibration (executed in OxCal 4.4⁵⁷ with IntCal20⁶⁵; making use of the vertically ordinal Sequence-formulation of its Chronological Query Language) was set up for subregional data clusters (supplementary information⁴⁹ section 1). The rationale for doing so³² is that the density of sampling allows the sorting of spatial selections of data points based on RSL age–depth position, exploiting the continuous RSL rise tendencies^{16,66} of basal peats. Applying a priori stratigraphic ordering reduced the 2σ age range of the legacy data (52 dates from samples collected before 2010) from 766 years to 459 years (40% reduction), and the 2σ age range of the post-2010 data ($N = 87$) from 422 years to 327 years (22% reduction). Extended Data Fig. 2 shows that including Bayesian age calibration had a small impact on P2, but for P1 peak rates increased almost 1 mm yr⁻¹ and the midpoint shifted by a century.

Selecting GIA models (step 3)

To investigate which drivers contribute to the RSL signal across the southern North Sea, we used both 1D and 3D global GIA models to produce RSL predictions. All models (1) require an input ice-sheet reconstruction, which defines the spatial and temporal history of major grounded ice sheets during the last glacial period, and (2) solve the generalized sea-level equation by including time-dependent shoreline migration as well as sea-level change in regions of ablating marine-based ice⁶⁷. Only the 1D GIA models include the influence of rotation of Earth on the sea-level calculation^{68,69}. However, comparison of the results from the 1D GIA model with and without rotation showed negligible differences across the study period. The main difference between the 1D and 3D models is in the approach used for the calculation of the deformation of Earth (that is, the Earth model). In the 3D GIA model, the viscosity varies both laterally and with depth, whereas in the 1D GIA model, viscosity varies only with depth.

We used ICE6G_5C¹⁰ (labelled as ICE6G) as the background input ice-sheet reconstruction to define the history for the NAISC and the AIS. This background reconstruction was combined with two reconstructions for the EuS (consisting of the Scandinavian, Barents–Kara Sea, British–Irish and North Sea ice sheets): (1) ICE6G and (2) BRITICE-CHRONO^{14,70}. The ICE6G EuS model was developed

iteratively using a 1D GIA model to capture the signal in the $\delta^{18}\text{O}$ curve and far-field sea-level data¹⁰. The BRITICE-CHRONO EuS model was developed independently of GIA modelling. Using a plastic ice-sheet model⁷¹, the spatial and temporal history of the ice sheet was constrained to fit geomorphological and geochronological information (see ref. 14).

The 1D GIA model adopts a spherically symmetrical Maxwell viscoelastic Earth model with three user-defined parameters: lithosphere thickness (km) and upper- and lower-mantle viscosity (Pa s). To investigate the optimum set of 1D Earth model parameters for each input EuS reconstruction, we used 1D Earth models with two lithosphere thickness values (71 km and 96 km) combined with upper- and lower-mantle viscosities in the range of 0.1×10^{21} Pa s to 1×10^{21} Pa s and 1×10^{21} Pa s to 50×10^{21} Pa s, respectively, which amounted to 108 models (Extended Data Table 1). As the model was run at a 0.5-ka temporal resolution from 122 ka to 0 ka, linear interpolation was used to produce predictions at the weighted mean age of each SLIP.

For the 3D GIA model, we used a finite-element model based on the method of ref. 72 with locally enhanced spatial resolution⁷³. The high-resolution zone is centred on the Southern North Sea and has spatial resolution of around 25 km. The resolution outside this zone is increasing from 50 km to 200 km. Present-day topography was obtained from ETOPO2v2⁷⁴. We investigated several 3D viscosity models, constructed with two approaches. The first approach converts seismic velocity anomalies (SMEAN2) to viscosity anomalies^{75,76}, using partial derivatives of seismic velocity to temperature that include anharmonic and anelastic effects⁷⁷. The conversion assumes that velocity anomalies are caused by thermal anomalies, although compositional anomalies could also have a role. Therefore, we vary a scale factor between 0 and 1 in steps of 0.25 to account for different contributions of mantle composition or temperature⁷⁷. The viscosity anomalies were added to the VM5a background viscosity profile¹⁰. The second approach uses an olivine flow law⁷⁸ for diffusion and dislocation creep to directly compute strain. With this approach, temporally variable viscosity can be incorporated, which is relevant because the effective viscosity becomes dependent on stress during dislocation creep. This is akin to, but not the same as, transient rheology, which has been investigated in other studies^{79,80}. The temperature of the upper 400 km is taken from the global lithosphere and upper-mantle WINTERC-G⁸¹ which relies on seismic data, gravity data and thermobarometric data to invert for temperature. The grain size and water content in the flow laws were varied over a range (1 mm to 10 mm, and 0 ppm, 500 ppm and 1,000 ppm)⁸². In total, 31 3D GIA model runs were created.

To evaluate which of the 1D and 3D viscosity profiles, when combined with the two input EuS ice-sheet reconstructions (ICE6G and BRITICE-CHRONO), was most suitable for the study region, we calculated the chi-square misfit (Extended Data Table 1) for the range of Earth models and the 109 SLIP RSL observations using:

$$\chi^2 = \frac{1}{n} \sum_{i=1}^n \left(\frac{o_i - m_i}{\sigma_i} \right)^2 \quad (1)$$

Here, o_i and m_i are the observed and predicted RSL, n is the total number of data points and σ_i is the 1σ RSL error. We have ignored time errors as they are small and uniform and will not lead to different selection of best-fit models. Applying a 95% confidence limit (calculated from an F -test) to identify a misfit region within which the best-fit models are found (red contours in EDF4) delimits a parameter space of only seven possible 1D upper- and lower-mantle viscosities. The selection of models is small as the SLIP data are sensitive to the choice of upper-mantle viscosity, a result that has been found for other regional RSL datasets as well¹⁴. The lowest misfits are associated with BRITICE-CHRONO ice-sheet reconstruction, with optimum parameters being a lithosphere thickness of 96 km, an upper-mantle viscosity of 0.3×10^{21} Pa s and a lower-mantle viscosity between 20×10^{21} Pa s and

50×10^{21} Pa s. The ICE6G reconstruction prefers a weaker lower-mantle viscosity, with values between 2×10^{21} Pa s and 5×10^{21} Pa s combined with an upper-mantle viscosity of 0.5×10^{21} Pa s, which is not surprising as this is close to the VM5a Earth model that was used in the creation of ICE6G¹⁰.

For several reasons, the misfit of the 31 3D viscosity models was notably larger than for the 1D models. One reason is related to the input seismic data that constrain the spatial pattern of the 3D viscosity model. Any errors in this dataset and in the conversion approach applied to it will directly translate into a worse misfit, which is only partially compensated by varying the scale factors or material parameters. Second, the ICE6G ice reconstruction is developed with the 1D Earth model VM5a, which means that 3D models probably have a worse fit than VM5a. Despite the larger misfit, we decided to also include the best-performing 3D GIA model in subsequent analyses, in an attempt to address any bias towards the assumption of a 1D rheology, as it is known from seismic models^{83,84} that lateral variations in Earth structure probably exist in and around Scandinavia, the North Sea and the British Isles.

The model runs that included stress-dependent rheology, which reduces viscosity when ice loading is applied, did not perform well. Therefore, we conclude that transient viscosity with a lower short-term viscosity would probably also not be preferred by the data. The 3D viscosity (Extended Data Fig. 5) and ice-sheet reconstruction with the lowest misfit come from ICE6G combined with the 3D Earth model SM9925 (SMEAN2 in combination with a scale factor of 0.25). In this profile, the viscosity decreases from Scandinavia to the west, reflecting the transition from the Scandinavian craton to the hotspot environment of Iceland. Viscosity also decreases southwards into the North Sea region. The lithosphere is not explicitly defined but follows from the effective viscosity; the larger viscosities beneath Scandinavia correspond to larger effective lithosphere thickness there.

In a next step, the eight selected distinct GIA models were selected to calculate the contribution of the EuS to the SLIP observed RSL at the location of each data point and to calculate the residual sea-level signal (supplementary information⁴⁹ section 4): five Earth models (four 1D and one 3D) combined with the ICE6G ice-sheet reconstruction and three 1D models combined with BRITICE-CHRONO ice-sheet reconstruction.

Isolating the EuS signal (step 4)

The GIA-modelled RSL signal consists of major contributions from the EuS and the NAISC, and a relatively small contribution from the AIS (Extended Data Fig. 6). Breaking down the individual contributions as a percentage of the total signal (Extended Data Figs. 7d–k and 8), it is apparent that the spatial variation in the observed GIA signal is primarily controlled by the forebulge generated by the EuS, with the two input ice-sheet reconstructions (ICE6G and BRITICE-CHRONO) producing different orientations and positions (Extended Data Fig. 6b,c). The EuS is by far the largest contributor to the total RSL, with more than 50% at all sites (Extended Data Figs. 7 and 8). In contrast, the AIS contributes between 0.2% and 16%, lowest for sites near the present-day coastline. Although the NAISC is predicted to contribute up to 45% for the older sites in the central North Sea, it is always smaller than the EuS contribution. Its spatial variation across the offshore SLIP-covered region, mainly caused by gravitational and water loading effects, at any time is small (Extended Data Fig. 8).

We define that the predicted sea level (total predicted_{rsl}) at any given latitude (θ), longitude (φ) and time (t) can be separated into the predicted (p) contributions from the major ice sheets:

$$\begin{aligned} \text{Total predicted}_{\text{rsl}}(\theta, \varphi, t) \\ = \text{pNAISC}_{\text{rsl}}(\theta, \varphi, t) + \text{pAIS}_{\text{rsl}}(\theta, \varphi, t) + \text{pEuS}_{\text{rsl}}(\theta, \varphi, t) \end{aligned} \quad (2)$$

Using equation (2), we calculated both the observed (obsEuS_{rsl}) and predicted (pEuS_{rsl}) EuS signal by subtracting the predicted contribution from the NAISC (pNAISC_{rsl}) (Extended Data Fig. 7e,g) and the AIS

(pAIS_{rsi}) (Extended Data Fig. 7d,f) from both the observed (Extended Data Fig. 7a) and predicted total RSL (Extended Data Fig. 7b,c):

$$\text{obsEuS}_{\text{rsi}}(\theta, \varphi, t) = \text{obs}_{\text{rsi}}(\theta, \varphi, t) - \text{pNAISC}_{\text{rsi}}(\theta, \varphi, t) - \text{pAIS}_{\text{rsi}}(\theta, \varphi, t) \quad (3)$$

$$\text{pEuS}_{\text{rsi}}(\theta, \varphi, t) = \text{total predicted}_{\text{rsi}}(\theta, \varphi, t) - \text{pNAISC}_{\text{rsi}}(\theta, \varphi, t) - \text{pAIS}_{\text{rsi}}(\theta, \varphi, t) \quad (4)$$

For equations (3) and (4), we used the predicted RSL from the eight models mentioned above (Extended Data Fig. 7d–g and Extended Data Table 1). We calculated the absolute misfit (in metres) between the predicted and observed EuS to assess how well the EuS signal is captured across our study region (Fig. 3).

Residual RSL change (step 5)

To calculate residual RSL change for the North Sea region, we first isolated the combined NAISC and AIS contribution to the RSL at each SLIP location using

$$\text{obsNAISC} + \text{AIS}_{\text{rsi}}(\theta, \varphi, t) = \text{obs}_{\text{rsi}}(\theta, \varphi, t) - \text{average}[\text{pEuS}_{\text{rsi}}(\theta, \varphi, t)] \quad (5)$$

The uncertainty in obs_{rsi} is taken from the HOLSEA database, whereas for average[pEuS], the standard deviation calculated from the eight GIA models is used as a measure of uncertainty. From the resulting data series (supplementary information⁴⁹ section 4), we calculated residual RSL and rates of residual RSL change with the EIV-IGP model^{37,38} (Extended Data Fig. 9), showing 26.3 m (2σ range, 23.8–28.8 m) of residual SLR for the 11–3 ka period (Fig. 4a).

Ice-sheet contributions (step 6)

Volumes of ice melt produced by ice sheets can be expressed in metres SLE, which is the average rise of global sea level if the volume is spread evenly across the world ocean surface. Step 6 considered the SLE contributions of the EuS, NAISC and AIS, for both the period 11–3 ka and the entire Holocene (11.7–0 ka), reviewed from published data, independent of global GIA or sea-level modelling. To convert melted ice volume (km³) to metres SLE we used the average (2.51 m per 10⁶ km³) of published values⁸⁵.

At its maximum extent during the last glacial, the EuS consisted of three main sectors⁴⁶: the British–Irish Ice Sheet, the Fennoscandian or Scandinavian Ice Sheet, and the Svalbard–Barents–Kara Ice Sheet. At the start of the Holocene, however, the British–Irish Ice Sheet and the Svalbard–Barents–Kara Ice Sheet were almost gone. The Fennoscandian Ice Sheet contributed meltwater to the GMSL rise until about 10 ka (refs. 46–48). Three studies^{46–48} indicate that the EuS-derived SLE was 2.2 m (2σ range, 1.5–2.9 m) between 11 ka and 10 ka and 3.0 m (2σ range, 2.1–4.3 m) between 11.7 ka and 10 ka (supplementary information⁴⁹ section 4).

Contributions from the NAISC were calculated using a recently published reconstruction of its extent through the Holocene⁸. Mapped NAISC areal extents (*A* in km²) at specific time slices from this Holocene reconstruction were converted to ice volume (*V* in km³) using a relationship for dome-shaped ice-sheet sectors⁸⁶: $\log V = 1.25(\log A - 1.13)$. This relationship has been used for parts of the NAISC⁸⁷, but not yet for all its sectors. The ice-volume uncertainty was calculated using published estimates of uncertainty in ice-sheet extent per time⁸. As an example, for 11 ka this means that the minimum ice-sheet volume equals the reconstructed ice-sheet volume for 10.3 ka and the maximum ice-sheet volume equals the volume of 11.8 ka (Table 1 in ref. 8).

The published volume–area relationship⁸⁶, however, was developed for a single ice sheet with one dome in the centre, whereas the NAISC initially consisted of interconnected ice sheets with multiple domes

(that is, Greenland and Innuitian ice sheets; Foxe–Baffin, Labrador and Keewatin domes of the Laurentide Ice Sheet). Only after the events that led to P2 did these respective sectors become fully disconnected^{8,88}. Applying the volume–area relationship of ref. 86 in a situation of interconnected ice sheets would lead to an overestimate of the volume in ice, as this would imply one very high dome in the centre of the interconnected area. An alternative approach would be to first split the interconnected ice sheets into subareas surrounding the individual domes and use the area–volume relationship. This leads, however, to an underestimation of the total volume in ice, as this would imply zero thickness at the edges of the ice sheets, whereas in reality, saddles with considerable thickness were present. As a compromise, we used both approaches for the time frames with interconnection (everything before 8.5 ka) and then averaged the resulting changes in ice volumes as an approximation of the contribution of the NAISC to the GMSL. Summing this to an ice-volume history suggests that the NAISC contained 40.8 m SLE (2σ range, 31.6–50.0 m) at 11.7 m SLE and 36.5 m SLE (2σ range, 30.2–42.8 m) at 11 ka. By 3 ka, the remaining NAISC ice volume was 6.8 m SLE (mostly Greenland Ice Sheet; 2σ range, 6.8–6.9 m), which makes for a NAISC contribution of 29.7 m SLE (2σ range, 23.4–35.6 m) between 11 ka and 3 ka, and 34.0 m SLE (2σ range, 24.8–43.2 m) over the entire Holocene (supplementary information⁴⁹ section 4). As a validity check, we compared our results with a recent global ice-sheet reconstruction (PaleoMIST1.0)⁸⁹ that gives ice-volume changes per 2.5 kyr (about 10 times coarser than our main results based on North Sea observations and about 5 times coarser than the NAISC reconstruction above based on volume–area relations). For the NAISC, the PaleoMIST reconstruction⁸⁹ shows a linear decrease in loss of volume between 17.5 ka and 5 ka that suggests that 33.3 m SLE has been lost since 11.7 ka, and 28.1 m after 11 ka, in agreement with our review and calculation.

To calculate the contribution of the AIS to GMSL, we used recent ensembles of deglacial simulations that are constrained by geological observations¹². We used the ten top-scoring simulations highlighted in that paper to calculate a median contribution from the AIS of 7.8 m SLE between 11 ka and 3 ka (2σ range, 4.1–9.6 m SLE; supplementary information⁴⁹ section 4). For the duration of the entire Holocene, our calculations show 8.1 m SLE (2σ range, 5.2–9.8 m SLE). All of these simulations indicate that the AIS was smaller than present at some point during the Holocene.

For the period 11–3 ka, the combined EuS–NAISC–AIS contribution is then 39.7 m (2σ range, 32.3–46.3 m). For the entire Holocene, it is 45.1 m (2σ range 35.4–54.6 m).

Global mean SLR (step 6)

In the North Sea (midpoint of our offshore data), residual RSL rise amounts 26.3 m (2σ range, 23.8–28.8) between 11 ka and 3 ka because of ice melt on the NAISC and the AIS. Globally, this value would be different from region to region, as a consequence of GIA effects, including gravitation⁹⁰. The spatial pattern in SLR across the world ocean and its marginal seas, which is generated as an output of global GIA modelling, is known as the fingerprint. It can in turn be broken down into component fingerprints for mass changes of respective ice-sheet complexes, be it the NAISC and the AIS in the early Holocene, or the Greenland Ice Sheet and the AIS in the modern situation. For a given increase of global-ocean volume in metres SLE coming from single or multiple mass sources, the fingerprint can be expressed as a percentage of GMSL rise (less than 100% of GMSL rise in the near to intermediate field; more than 100% in the far field). Relative fingerprint maps have also been used inversely, for instance, to identify the source of meltwater pulses⁴³ and to convert locally reconstructed magnitudes of sea-level jumps (metres RSL change), to equivalent globally averaged magnitudes (metres SLE^{40,91,92}).

We applied such inversion to assess GMSL between 11 ka and 3 ka. During this time, the source of GMSL rise was the NAISC for about three-quarters of the total GMSL (Fig. 4). As the composite fingerprint

of the NAISC, the AIS and other potential sources is a mass-weighted one, the NAISC fingerprint will be dominant in the North Sea region. This also goes for sensitivity to mass changes and shifts of the NAISC mass centre during early Holocene deglaciation, as the NAISC is more proximal to the North Sea than the AIS. The dominance can be expected to disappear at some point within the middle Holocene (8.2–4.2 ka, probably after 7 ka) when NAISC deglaciation was completed, with the Greenland ice mass surviving and stabilizing^{8,88}. A direct comparison of GMSL curves from ICE6G¹⁰ and PaleoMIST⁸⁹ with both the observed (geological data) and predicted RSL (GIA modelling with all ice sheets) for our SLIP locations shows the GMSL to lie well above North Sea RSL, especially in the early Holocene (Extended Data Fig. 10a–d), reflecting the strong GIA signal from the nearby EuS. Extended Data Fig. 10 also shows that the predicted RSL (Extended Data Fig. 10c,d) has much greater scatter than the observed RSL (Extended Data Fig. 10a,b), highlighting the uncertainty within the GIA modelling output when predicting RSL for areas near former ice sheets. After removal of the EuS signal in the RSL data, both GMSL curves now plot below the North Sea residual RSL data as a result of the combined NAISC–AIS fingerprint (Extended Data Fig. 10e,f).

To assess this fingerprint for the 11–8 ka period, the model predictions for each SLIP location (excluding the EuS signal) were divided by the GMSL value for the time the SLIP was formed. This shows that the North Sea region captured 74% (2σ range, 68–90%; Extended Data Fig. 11) of the GMSL signal in the early Holocene. Extended Data Fig. 11 shows scatter in the fingerprint result (reflecting uncertainties in the GIA modelling), but also suggests that the average ratio is slowly dropping with time.

The drop in fingerprint with time may well reflect further continued early Holocene mass-centre shifting within the NAISC, from a position over central Canada to one over Greenland. The 74% ratio falls in between the GIA-modelled fingerprint of the NAISC around 14.65 ka (about 80%, meltwater pulse 1A) for the North Sea⁴³ and the modelled fingerprint of 70% for the 8.5–8.2 ka Lake Agassiz–Ojibway drainage events in this region⁹³. These differences are explained by the fact that for 14.65 ka the western part of the NAISC was the modelled source area (at greater distance from the North Sea), whereas for 8.5–8.2 ka, the southeastern part of the NAISC is the source area (closer to the North Sea).

This fingerprint ratio, including the 2σ range, was then used to translate the 26.3 m (2σ range, 23.8–28.8 m; 74%) residual SLR in the North Sea region to a global NAISC–AIS signal of 35.5 m (2σ range 27.1–40.0 m; 100%). Adding the EuS contribution of 2.2 m SLE (2σ range 1.5–2.9 m; see below) after 11 ka results in a total GMSL rise of 37.7 m (2σ range, 29.3–42.2 m) between 11 ka and 3 ka (Fig. 4a). In a next iterative round of running 1D and 3D GIA models, temporal variability of the GMSL fingerprint on the North Sea residual RSL signal may be re-evaluated by tuning GIA model simulations, including an updated NAISC, to sea-level data. This should improve the match between fingerprint-corrected GMSL curves and the geological sea-level observations. Such an optimization was beyond the scope of the current work.

Additional details and references regarding the methods^{2,8,10,14,16,23,25,32,33,46–48,57–66,86,88,91,94–179} are available in supplementary information⁴⁹.

Data availability

The supplementary information has four sections with data and additional information, hosted on Zenodo at <https://doi.org/10.5281/zenodo.10801302> (ref. 49). It contains (1) the RSL database, Bayesian calibration scripts and technical documentation; (2) core photographs, XRF and diatom analysis; (3) background-subsidence grids and technical documentation, and (4) regional GIA modelling output, residual sea-level data and calculated temporal changes in ice-sheet volume for the three major ice sheets.

Code availability

The code used to run the EIV-IGP model is available at https://github.com/ncahill89/EIV_IGP/blob/master/RunIGP.R. We used the following settings in the code: ‘BP_age_scale = TRUE’; ‘interval=80’ and ‘fast = FALSE’. GIA outputs and produced plots are available on request from S.L.B. and M.P.H., respectively.

52. *DINOloket (Internet Portal for Geo-Information)* (TNO, 2024); <https://www.dinoloeket.nl/en>.
53. *Niedersächsischen Bodeninformationssysteme* (NIBIS, 2024); <https://nibis.lbeg.de/cardo/map3?7TH=PROFILBKBOHRSEBOHRGEBBOHRHYBOHRIGBOHR1447599>.
54. Reinhardt, L. & Vink, A. *RV Celtic Explorer North Sea Cruise 2009—Geology and Geophysics Geopotenzial Deutsche Nordsee Project BGR, LBEg and BSH Report* (BGR, 2009).
55. Reinhardt, L. & Lutz, R. *RV Celtic Explorer North Sea Cruise 2011—Geology and Geophysics Geopotenzial Deutsche Nordsee Project BGR, LBEg and BSH Report* (BGR, 2011).
56. De Haas, H. *North Sea Monitoring Texel—Texel, 16 June - 29 June 2017 NIOZ cruise report RV Pelagia cruise 64PE423* (2017).
57. Bronk Ramsey, C. Bayesian analysis of radiocarbon dates. *Radiocarbon* **51**, 337–360 (2009).
58. Van Asselen, S. *Peat Compaction in Deltas: Implications for Holocene Delta Evolution*. PhD dissertation, Utrecht Univ. (2010).
59. Uehara, K., Scourse, J. D., Horsburgh, K. J., Lambeck, K. & Purcell, A. P. Tidal evolution of the northwest European shelf areas from the Last Glacial Maximum to the present. *J. Geophys. Res.* **111**, C09025–C09025 (2006).
60. Van der Molen, J. & De Swart, H. E. Holocene tidal conditions and tide-induced sand transport in the southern North Sea. *J. Geophys. Res.* **C106**, 9339–9362 (2001).
61. Van der Molen, J. & Van Dijk, B. The evolution of the Dutch and Belgian coasts and the role of sand supply from the North Sea. *Glob. Planet. Change* **27**, 223–244 (2000).
62. Van de Plassche, O. *Sea-level Change and Water-level Movements in The Netherlands during the Holocene* PhD dissertation, Vrije Univ. (1982).
63. Van de Plassche, O. & Roep, T. B. in *Late Quaternary Sea-level Correlation and Applications* (eds Scott, D. B. et al.) 41–56 (Kluwer, 1989).
64. Cohen, K. M., Cartelle, V., Barnett, R., Busschers, F. S. & Barlow, N. L. M. Last Interglacial sea-level data points from Northwest Europe. *Earth Syst. Sci. Data* **14**, 2895–2937 (2022).
65. Reimer, P. J. et al. The IntCal20 Northern Hemisphere radiocarbon age calibration curve (0–55 cal kBP). *Radiocarbon* **62**, 725–757 (2020).
66. Van de Plassche, O. in *Sea-level Research: A Manual for the Collection and Evaluation of Data* (ed. Van de Plassche O.) 1–26 (Geobooks, 1986).
67. Kendall, R. A., Mitrovica, J. X. & Milne, G. A. On post-glacial sea level—II. Numerical formulation and comparative results on spherically symmetric models. *Geophys. J. Int.* **161**, 679–706 (2005).
68. Milne, G. A. & Mitrovica, J. X. Postglacial sea-level change on a rotating Earth. *Geophys. J. Int.* **133**, 1–19 (1998).
69. Mitrovica, J. X., Milne, G. A. & Davis, J. L. Glacial isostatic adjustment on a rotating earth. *Geophys. J. Int.* **147**, 562–578 (2001).
70. Clark, C. D. et al. Growth and retreat of the last British–Irish Ice Sheet, 31000 to 15000 years ago: the BRITICE-CHRONO reconstruction. *Boreas* **51**, 699–758 (2022).
71. Gowan, E. J. et al. ICESHEET 1.0: a program to produce paleo-ice sheet reconstructions with minimal assumptions. *Geosci. Model Dev.* **9**, 1673–1682 (2016).
72. Wu, P. Using commercial finite element packages for the study of Earth deformations, sea levels and the state of stress. *Geophys. J. Int.* **158**, 401–408 (2004).
73. Blank, B., Barletta, V., Hu, H., Pappa, F. & van der Wal, W. Effect of lateral and stress-dependent viscosity variations on GIA induced uplift rates in the Amundsen Sea Embayment. *Geochem. Geophys. Geosyst.* **22**, e2021GC009807 (2021).
74. NOAA National Geophysical Data Center. 2006: 2-minute gridded global relief data (etopo2) v2. NOAA National Centers for Environmental Information <https://doi.org/10.7289/V5J1012Q> (2023).
75. Ivins, E. R., Van der Wal, W., Wiens, D. A., Lloyd, A. J. & Caron, L. Antarctic upper mantle rheology. *Geol. Soc. Lond. Mem.* **56**, 267–294 (2023).
76. Karato, S.-I. *Deformation of Earth Materials: An Introduction to the Rheology of Solid Earth* (Cambridge Univ. Press, 2008).
77. Wu, P., Wang, H. & Steffen, H. The role of thermal effect on mantle seismic anomalies under Laurentia and Fennoscandia from observations of glacial isostatic adjustment. *Geophys. J. Int.* **192**, 7–17 (2012).
78. Hirth, G. & Kohlstedt, D. in *Inside the Subduction Factory* (ed. Eiler, J.) 83–105 (American Geophysical Union, 2004).
79. Lau, H. C. P. Transient rheology in sea level change: implications for meltwater pulse 1A. *Earth Planet. Sci. Lett.* **609**, 118106 (2023).
80. Simon, K. M., Riva, R. E. M. & Broerse, T. Identifying geographical patterns of transient deformation in the geological sea level record. *J. Geophys. Res. Solid Earth* **127**, e2021JB023693 (2022).
81. Fulla, J., Lebedev, S., Martinec, Z. & Celli, N. L. WINTERC-G: mapping the upper mantle thermochemical heterogeneity from coupled geophysical–petrological inversion of seismic waveforms, heat flow, surface elevation and gravity satellite data. *Geophys. J. Int.* **226**, 146–191 (2021).
82. Wal, W. V. D. et al. Glacial isostatic adjustment model with composite 3-D Earth rheology for Fennoscandia. *Geophys. J. Int.* **194**, 61–77 (2013).
83. Celli, N. L., Lebedev, S., Schaeffer, A. J. & Gaina, C. The tilted Iceland Plume and its effect on the North Atlantic evolution and magmatism. *Earth Planet. Sci. Lett.* **569**, 117048 (2021).
84. Debayle, E., Dubuffet, F. & Durand, S. An automatically updated S-wave model of the upper mantle and the depth extent of azimuthal anisotropy. *Geophys. Res. Lett.* **43**, 674–682 (2016).
85. Simms, A. R., Lisiecki, L., Gebbie, G., Whitehouse, P. L. & Clark, J. F. Balancing the last glacial maximum (LGM) sea-level budget. *Quat. Sci. Rev.* **205**, 143–153 (2019).

86. Paterson, W. S. B. *The Physics of Glaciers* (Pergamon, 1994).
87. Ullman, D. J. et al. Final Laurentide ice-sheet deglaciation and Holocene climate-sea level change. *Quat. Sci. Rev.* **152**, 49–59 (2016).
88. Dalton, A. S. et al. Deglaciation of the North American ice sheet complex in calendar years based on a comprehensive database of chronological data: NADI-1. *Quat. Sci. Rev.* **321**, 108345 (2023).
89. Gowan, E. J. et al. A new global ice sheet reconstruction for the past 80000 years. *Nat. Commun.* **12**, 1199 (2021).
90. Milne, G. A., Gehrels, W. R., Hughes, C. W. & Tamisiea, M. E. Identifying the causes of sea-level change. *Nat. Geosci.* **2**, 471–478 (2009).
91. Hijma, M. P. & Cohen, K. M. Timing and magnitude of the sea-level jump precluding the 8200 yr event. *Geology* **38**, 275–278 (2010).
92. Törnqvist, T. E. & Hijma, M. P. Links between early Holocene ice-sheet decay, sea-level rise and abrupt climate change. *Nat. Geosci.* **5**, 601–606 (2012).
93. Kendall, R. A., Mitrovica, J. X., Milne, G. A., Törnqvist, T. E. & Li, Y. The sea-level fingerprint of the 8.2 ka climate event. *Geology* **36**, 423–426 (2008).
94. Argus, D. F., Peltier, W. R., Drummond, R. & Moore, A. W. The Antarctica component of postglacial rebound model ICE-6G_C (VM5a) based on GPS positioning, exposure age dating of ice thicknesses, and relative sea level histories. *Geophys. J. Int.* **198**, 537–563 (2014).
95. Hijma, M. P. et al. in *Handbook of Sea-Level Research* (eds Shennan, I. et al.) 536–553 (Wiley-Blackwell, 2015).
96. Alappat, L., Vink, A., Tsukamoto, S. & Frechen, M. Establishing the Late Pleistocene–Holocene sedimentation boundary in the southern North Sea using OSL dating of shallow continental shelf sediments. *Proc. Geol. Assoc.* **121**, 43–54 (2010).
97. Baeteman, C., Waller, M. & Kiden, P. Reconstructing middle to late Holocene sea-level change: a methodological review with particular reference to 'A new Holocene sea-level curve for the southern North Sea' presented by K.-E. Behre. *Boreas* **40**, 557–572 (2011).
98. Barckhausen, J. *Geologische Karte von Niedersachsen 1:25000, Blatt 2609 Emden* (NLFb Hannover, 1984).
99. Behre, K.-E. Eine neue Meeresspiegelkurve für die südliche Nordsee. *Probleme der Küstenforschung im südlichen Nordseegebiet* **28**, 9–63 (2003).
100. Behre, K.-E. *Die ursprüngliche Vegetation in den deutschen Marschgebieten und deren Veränderung durch prähistorische Besiedlung und Meeresspiegelbewegungen* Vol. 13, 85–96 (Gesellschaft für Ökologie, 1985).
101. Behre, K.-E., Menke, B. & Streif, H. The quaternary geological development of the German part of the North Sea. *Acta Univ. Ups. Symp. Univ. Ups. Annum Quingentesimum Celebrantis* **2**, 85–113 (1979).
102. Bos, I. J., Busschers, F. S. & Hoek, W. Z. Organic-facies determination: a key for understanding facies distribution in the basal peat layer of the Holocene Rhine–Meuse delta, The Netherlands. *Sedimentology* **59**, 676–703 (2012).
103. Brain, M. J. et al. Modelling the effects of sediment compaction on salt marsh reconstructions of recent sea-level rise. *Earth Planet. Sci. Lett.* **345–348**, 180–193 (2012).
104. Bungenstock, F., Freund, H. & Bartholomä, A. Holocene relative sea-level data for the East Frisian barrier coast, NW Germany, southern North Sea—CORRIGENDUM. *Neth. J. Geosci.* **101**, e2 (2022).
105. Bungenstock, F., Freund, H. & Bartholomä, A. Holocene relative sea-level data for the East Frisian barrier coast, NW Germany, southern North Sea. *Neth. J. Geosci.* **100**, e16 (2021).
106. Clerckx, A. P. P. M. et al. *Broekbossen van Nederland* IBN-Report 096 (Instituut voor Bos- en Natuuronderzoek, 1994).
107. Cohen, K. M. in *River Deltas: Concepts, Models, and Examples* SEPM Special Publication Vol. 83 (eds Giosan, L. & Bhattacharaya, J. P.) 341–364 (Society for Sedimentary Geology, 2005).
108. De Haas, T. et al. Holocene evolution of tidal systems in The Netherlands: effects of rivers, coastal boundary conditions, eco-engineering species, inherited relief and human interference. *Earth Sci. Rev.* **177**, 139–163 (2018).
109. Heaton, T. J. et al. Marine20—the marine radiocarbon age calibration curve (0–55,000 cal BP). *Radiocarbon* **62**, 779–820 (2020).
110. Nougues, L. *Bodemdalingsmonitor 2022 Kustfundament en getijdenbekkens—Bodemdeling en GNSS-stations* Deltares Report 11208035-003-ZKS-0004 (Deltares, 2022).
111. Hijma, M. P. & Van Onselen, E. *Bodemdalingsmonitor 2019—Kustfundament en de getijdenbekkens* Deltares Report 11203683-002-ZKS-0017 (Deltares, 2019).
112. Hijma, M. P., Cohen, K. M., Hoffmann, G., Van der Spek, A. J. F. & Stouthamer, E. From river valley to estuary: the evolution of the Rhine mouth in the early to middle Holocene (western Netherlands, Rhine–Meuse delta). *Neth. J. Geosci.* **88**, 13–53 (2009).
113. Jelgersma, S. Holocene sea-level changes in The Netherlands. *Mededelingen Geologische Stichting* **7**, 1–101 (1961).
114. Konradi, P. B. Biostratigraphy and environment of the Holocene marine transgression in the Heligoland Channel, North Sea. *Bull. Geol. Soc. Den.* **47**, 71–79 (2000).
115. Kooi, H., Johnston, P., Lambeck, K., Smither, C. & Ronald, M. Geological causes of recent (–100yr) vertical land movement in The Netherlands. *Tectonophysics* **299**, 297–316 (1998).
116. Koster, K., De Lange, G., Harting, R., de Heer, E. & Middelkoop, H. Characterizing void ratio and compressibility of Holocene peat with CPT for assessing coastal–deltaic subsidence. *Q. J. Eng. Geol. Hydrogeol.* **51**, 210 (2018).
117. Koster, K., Stafleu, J. & Cohen, K. M. Generic 3D interpolation of Holocene base-level rise and provision of accommodation space, developed for the Netherlands coastal plain and inflatted palaeovalleys. *Basin Res.* **29**, 775–797 (2017).
118. Krüger, S., Dörfler, W., Bennike, O. & Wolters, S. Life in Doggerland—palynological investigations of the environment of prehistoric hunter-gatherer societies in the North Sea Basin. *E&G Quat. Sci. J.* **66**, 3–13 (2017).
119. Linke, G. Der Ablauf der holozänen Transgression der Nordsee aufgrund von Ergebnissen aus dem Gebiet Neuwerk/Scharhörn. *Probleme der Küstenforschung im südlichen Nordseegebiet* **14**, 123–157 (1982).
120. Ludwig, G., Müller, H. & Streif, H. New dates on Holocene sea level changes in the German Bight. *Spec. Publ. Int. Assoc. Sediment.* **5**, 211–219 (1981).
121. Ludwig, G., Müller, H. & Streif, H. Neuere Datum zum holozänen Meeresspiegelanstieg im Bereich der Deutschen Bucht. *Geol. Jahrb. D* **32**, 3–22 (1979).
122. Meijles, E. W. et al. Holocene relative mean sea-level changes in the Wadden Sea area, northern Netherlands. *J. Quat. Sci.* <https://doi.org/10.1002/jqs.3068> (2018).
123. Makaske, B., Van Smeerdijk, D. G., Peeters, H., Mulder, J. R. & Spek, T. Relative water-level rise in the Flevo lagoon (The Netherlands), 5300–2000 cal. yr BC: an evaluation of new and existing basal peat time-depth data. *Neth. J. Geosci.* **82**, 115–131 (2016).
124. Menke, B. Befunde und Überlegungen zum nachheizeitlichen Meeresspiegelanstieg (Dithmarschen und Eiderstedt, Schleswig-Holstein). *Probleme der Küstenforschung im südlichen Nordseegebiet* **11**, 145–161 (1976).
125. Menke, B. in *Deutsche Beiträge zur Quartärforschung in der südlichen Nordsee* Geologisches Jahrbuch Vol. A146 (ed. Streif, H.) 177–182 (Bundesanstalt für Geowissenschaften und Rohstoffe und den Staatlichen Geologischen Diensten in der Bundesrepublik Deutschland, 1996).
126. Oele, E. The Quaternary geology of the Dutch part of the North Sea, north of the Frisian Isles. *Geol. Mijnbouw* **48**, 467–480 (1969).
127. Preuss, H. Die holozäne Entwicklung der Nordseeküste im Gebiet der östlichen Wesermarsch. *Geol. Jahrb.* **53**, 1–89 (1979).
128. Reynaud, J.-Y. & Dalrymple, R. W. in *Principles of Tidal Sedimentology* (eds Davis, R. A. Jr & Dalrymple, R. W.) 335–369 (Springer, 2012).
129. Schaumann, R. M. et al. The Middle Pleistocene to early Holocene subsurface geology of the Norderney tidal basin: new insights from core data and high-resolution sub-bottom profiling (Central Wadden Sea, southern North Sea). *Neth. J. Geosci.* **100**, e15 (2021).
130. Schlütz, F., Enters, D. & Bittmann, F. From dust till drowned: the Holocene landscape development at Norderney, East Frisian Islands. *Neth. J. Geosci.* **100**, e7 (2021).
131. Shennan, I. et al. Holocene isostasy and relative sea-level changes on the east coast of England. *Geol. Soc. Lond. Spec. Publ.* **166**, 275–298 (2000).
132. Streif, H. *Geologische Karte von Niedersachsen 1:25 000, Blatt 2314 Hooksiel* (NLFb Hannover, 1985).
133. Streif, H., Uffenorde, H. & Vinken, R. *Untersuchungen zum pleistozänen und holozänen Transgressionsgeschehen im Bereich der südlichen Nordsee* (Niedersächsisches Landesamt für Bodenforschung, 1983).
134. Törnqvist, T. E., van Ree, M. H. M., van 't Veer, R. & van Geel, B. Improving methodology for high-resolution reconstruction of sea-level rise and neotectonics by paleoecological analysis and AMS ¹⁴C dating of basal peats. *Quat. Res.* **49**, 72–85 (1998).
135. Van Asselen, S., Cohen, K. M. & Stouthamer, E. The impact of avulsion on groundwater level and peat formation in delta floodbasins during the middle-Holocene transgression in the Rhine–Meuse delta, The Netherlands. *Holocene* **27**, 1694–1706 (2017).
136. Van Asselen, S., Karssenberg, D. & Stouthamer, E. Contribution of peat compaction to relative sea-level rise within Holocene deltas. *Geophys. Res. Lett.* **38**, L24401–L24401 (2011).
137. Van de Plassche, O. Evolution of the intra-coastal tidal range in the Rhine–Meuse delta and Flevo Lagoon, 5700–3000 yrs cal B.C. *Mar. Geol.* **124**, 113–128 (1995).
138. Van de Plassche, O., Bohncke, S. J. P., Makaske, B. & Van der Plicht, J. Water-level changes in the Flevo area, central Netherlands (5300–1500 BC): implications for relative mean sea-level rise in the Western Netherlands. *Quat. Int.* **133–134**, 77–93 (2005).
139. Van de Plassche, O., Makaske, B., Hoek, W. Z., Konert, M. & Van der Plicht, J. Mid-Holocene water-level changes in the lower Rhine–Meuse delta (western Netherlands): implications for the reconstruction of relative mean sea-level rise, palaeoriver-gradients and coastal evolution. *Neth. J. Geosci.* **89**, 3–20 (2010).
140. Van der Spek, A. J. F. *Large-scale Evolution of Holocene Tidal Basins in the Netherlands*. PhD dissertation, Utrecht Univ. (1994).
141. Vis, G.-J. et al. in *Handbook of Sea-Level Research* (eds Shennan, I. et al.) 514–535 (Wiley-Blackwell, 2015).
142. Vos, P. C., Bunnik, F. P. M., Cohen, K. M. & Cremer, H. A staged geogenetic approach to underwater archaeological prospection in the Port of Rotterdam (Yangtzehaven, Maasvlakte, The Netherlands): a geological and palaeoenvironmental case study for local mapping of Mesolithic lowland landscapes. *Quat. Int.* **367**, 4–31 (2015).
143. Wolters, S., Zeiler, M. & Bungenstock, F. Early Holocene environmental history of sunken landscapes: pollen, plant macrofossils and geochemical analyses from the Borkum Riffgrund, southern North Sea. *Int. J. Earth Sci.* **99**, 1707–1719 (2010).
144. Bloemsa, M. *Development of a Modelling Framework for Core Data Integration using XRF Scanning*. PhD thesis, Delft Univ. Technology (2015).
145. Arfai, J. et al. Rapid Quaternary subsidence in the northwestern German North Sea. *Sci. Rep.* **8**, 11524 (2018).
146. Cameron, T. D. J., Laban, C. & Schüttenhelm, R. T. E. *Quaternary Geology. Sheet 52°N–2°E, Flemish Bight 1:250.000 Series* (British Geological Survey, 1984).
147. Laban, C., Schüttenhelm, R. T. E., Balson, P. S., Baeteman, C. & Paeppe, R. *Quaternary Geology. Sheet 51°N–02°E, Ostend 1:250.000 Series* (British Geological Survey, 1992).
148. Deckers, J. et al. *Geologisch en hydrogeologisch 3D model van het Cenozoïcum van de Roerdaalslenk in Zuidoost-Nederland en Vlaanderen (H3O-Roerdaalslenk)* TNO-Report 2014 R10799 / VITO-Report 2014/ETE/R/1 (TNO, 2014).
149. *Teilmodell Quartär 3D. Bundesministerium für Wirtschaft und Technologie (BMW), Niedersächsischen Ministerium für Wirtschaft, Arbeit und Verkehr, Bundesministerium für Verkehr, Bau und Stadtentwicklung (BMVB/S) (GPDN, 2022); https://www.gpdn.de/.*
150. Jakob, K. A. et al. A new sea-level record for the Neogene/Quaternary boundary reveals transition to a more stable East Antarctic Ice Sheet. *Proc. Natl Acad. Sci. USA* **117**, 30980–30987 (2020).
151. Kopp, R. E., Simons, F. J., Mitrovica, J. X., Maloof, A. C. & Oppenheimer, M. Probabilistic assessment of sea level during the last interglacial stage. *Nature* **462**, 863–867 (2009).
152. Kuhlmann, G. et al. Chronostratigraphy of Late Neogene sediments in the southern North Sea Basin and paleoenvironmental interpretations. *Palaeogeogr. Palaeoclimatol. Palaeoecol.* **239**, 426–455 (2006).
153. Kuhlmann, G. et al. Integrated chronostratigraphy of the Pliocene–Pleistocene interval and its relation to the regional stratigraphical stages in the southern North Sea region. *Neth. J. Geosci.* **85**, 19–35 (2006).
154. Lamb, R. M., Harding, R., Hulse, M., Stewart, M. & Brocklehurst, S. H. The early Quaternary North Sea Basin. *J. Geol. Soc.* **175**, 275–290 (2018).

155. Lambeck, K. et al. Constraints on the Late Saalian to early Middle Weichselian ice sheet of Eurasia from field data and rebound modelling. *Boreas* **35**, 539–575 (2006).
156. *Generalised Quaternary Geological Map of Lower Saxony, 1:500 000—Depth of the Quaternary Base* (Landesamt für Bergbau, Energie und Geologie, 2022).
157. Nielsen, T., Mathiesen, A. & Bryde-Auken, M. Base Quaternary in the Danish parts of the North Sea and Skagerrak. *GEUS Bull.* **15**, 37–40 (2008).
158. Patruno, S. et al. Upslope-climbing shelf-edge clinoforms and the stepwise evolution of the northern European glaciation (lower Pleistocene Eridanos Delta system, UK North Sea): when sediment supply overwhelms accommodation. *Basin Res.* **32**, 224–239 (2020).
159. Rovere, A. et al. Documentation of the World Atlas of Last Interglacial Shorelines (WALIS). Zenodo <https://doi.org/10.5281/zenodo.3961543> (2020).
160. Digital Geological Model of the Shallow Subsurface of the Netherlands (DGM) version v2.2 (TNO-GDN, 2022); <https://www.dinoloket.nl/en/the-digital-geological-model-dgm> (2022).
161. Van der Meer, D. G., Scotese, C. R., Mills, B. J. W., Sluijs, A. & Van de Weg, R. M. B. Long-term Phanerozoic global mean sea level: insights from strontium isotope variations and estimates of continental glaciation. *Gondwana Res.* **111**, 103–121 (2022).
162. Vernes, R. W. et al. *Geologisch en hydrogeologisch 3D model van het Cenozoïcum van de Belgisch-Nederlandse grensstreek van Midden-Brabant / De Kempen (H30 – De Kempen)* TNO-Report 2017 R11261 / VITO-Report 2017/RMA/R/1348 (TNO, 2018).
163. Dellwig, O., Böttcher, M. E., Lipinski, M. & Brumsack, H.-J. Trace metals in Holocene coastal peats and their relation to pyrite formation (NW Germany). *Chem. Geol.* **182**, 423–442 (2002).
164. Goldberg, T. et al. Suitability of calibrated X-ray fluorescence core scanning for environmental geochemical characterisation of heterogeneous sediment cores. *Appl. Geochem.* **125**, 104824 (2021).
165. Guyard, H. et al. High-altitude varve records of abrupt environmental changes and mining activity over the last 4000 years in the Western French Alps (Lake Bramant, Grandes Rousses Massif). *Quat. Sci. Rev.* **26**, 2644–2660 (2007).
166. Hartley, B., Barber, H. G., Carter, J. R. & Sims, P. *An Atlas of British Diatoms* (Biopres, 1996).
167. Hemphill-Haley, E. *Taxonomy of Recent and Fossil (Holocene) Diatoms (Bacillariophyta) from Northern Willapa Bay*, Washington Report No. 2331-1258 (US Geological Survey, 1993).
168. Patrick, R. & Reimer, C. W. *The Diatoms of the United States. Volume 2, Part 1* Vol. 13 (Academy of Natural Sciences of Philadelphia, 1975).
169. Patrick, R. & Reimer, C. W. *The Diatoms of the United States. Volume 1* Vol. 13 (Academy of Natural Sciences of Philadelphia, 1966).
170. Palmer, A. J. M. & Abbott, W. H. in *Sea-Level Research: A Manual for the Collection and Evaluation of Data* (ed. van de Plassche, O.) 457–487 (Springer, 1986).
171. Tjallingii, R., Statterger, K., Wetzell, A. & Van Phach, P. Infilling and flooding of the Mekong River incised valley during deglacial sea-level rise. *Quat. Sci. Rev.* **29**, 1432–1444 (2010).
172. Van der Werff, A. & Huls, H. *Diatomeenflora van Nederland. 8 Parts* (Westzijde 13a, 1958).
173. Weltje, G. J. et al. in *Micro-XRF Studies of Sediment Cores: Applications of a Non-destructive Tool for the Environmental Sciences* (eds Croudace, I. W. & Guy Rothwell, R.) 507–534 (Springer, 2015).
174. Ziegler, M., Jilbert, T., de Lange, G. J., Lourens, L. J. & Reichert, G.-J. Bromine counts from XRF scanning as an estimate of the marine organic carbon content of sediment cores. *Geochem. Geophys. Geosyst.* <https://doi.org/10.1029/2007GC001932> (2008).
175. Zuther, M., Brockamp, O. & Clauer, N. Composition and origin of clay minerals in Holocene sediments from the south-eastern North Sea. *Sedimentology* **47**, 119–134 (2000).
176. Rieu, R., Van Heteren, S., Van der Spek, A. J. F. & De Boer, P. L. Development and preservation of a mid-Holocene tidal-channel network offshore the western Netherlands. *J. Sediment. Res.* **75**, 409–419 (2005).
177. Hijma, M. P., Van der Spek, A. J. F. & Van Heteren, S. Development of a mid-Holocene estuarine basin, Rhine–Meuse mouth area, offshore the Netherlands. *Mar. Geol.* **271**, 198–211 (2010).
178. Streif, H. *Geologische Karte von Niedersachsen 1:25 000, Blatt 2314 Wilhemshaven* (NLF Hannover, 1981).
179. Berendsen, H. J. A. et al. New groundwater-level rise data from the Rhine–Meuse delta—implications for the reconstruction of Holocene relative mean sea-level rise and differential land-level movements. *Neth. J. Geosci.* **86**, 333–354 (2007).

Acknowledgements We thank the crews of all the research cruises that we participated in when collecting the offshore samples; N. van Asch for macrofossil analysis of the cores collected with RV Pelagia; N. Janssen and S. de Vries for the description of the cores taken with RV Pelagia; and the Dutch Cultural Heritage Agency (Björn Smit) for discussion and financial support.

Author contributions G.-J.R. and S.v.H. initiated the 2017 data collection campaign aboard RV Pelagia, which grew into the interdisciplinary study presented here. M.P.H., F.S.B., N.L.M.B., K.M.C., K.F.R., P.K., B.L.M., L.R. and A.V. all contributed to fieldwork and sampling during this and other cruises. M.F. was in charge of the radiocarbon dating of samples from the German cruises. The Bayesian age calibration was designed and carried out by K.M.C. The XRF and diatom analyses were conducted by R.H. and N.L.M.B., respectively. The basin-subsidence grids were created by F.S.B., in collaboration with K.M.C. M.P.H. and K.M.C. analysed the data according to the HOLSEA protocol. S.L.B., W.v.d.W. and B.B. executed the GIA modelling and analysis. The statistical analysis of the sea-level data was executed by M.P.H. and A.M. M.P.H. wrote the paper with input from S.L.B., K.M.C., W.v.d.W., B.B., N.L.M.B., S.v.H. and F.S.B. All co-authors contributed to the data interpretation and to text revisions towards the final publication.

Competing interests The authors declare no competing interests.

Additional information

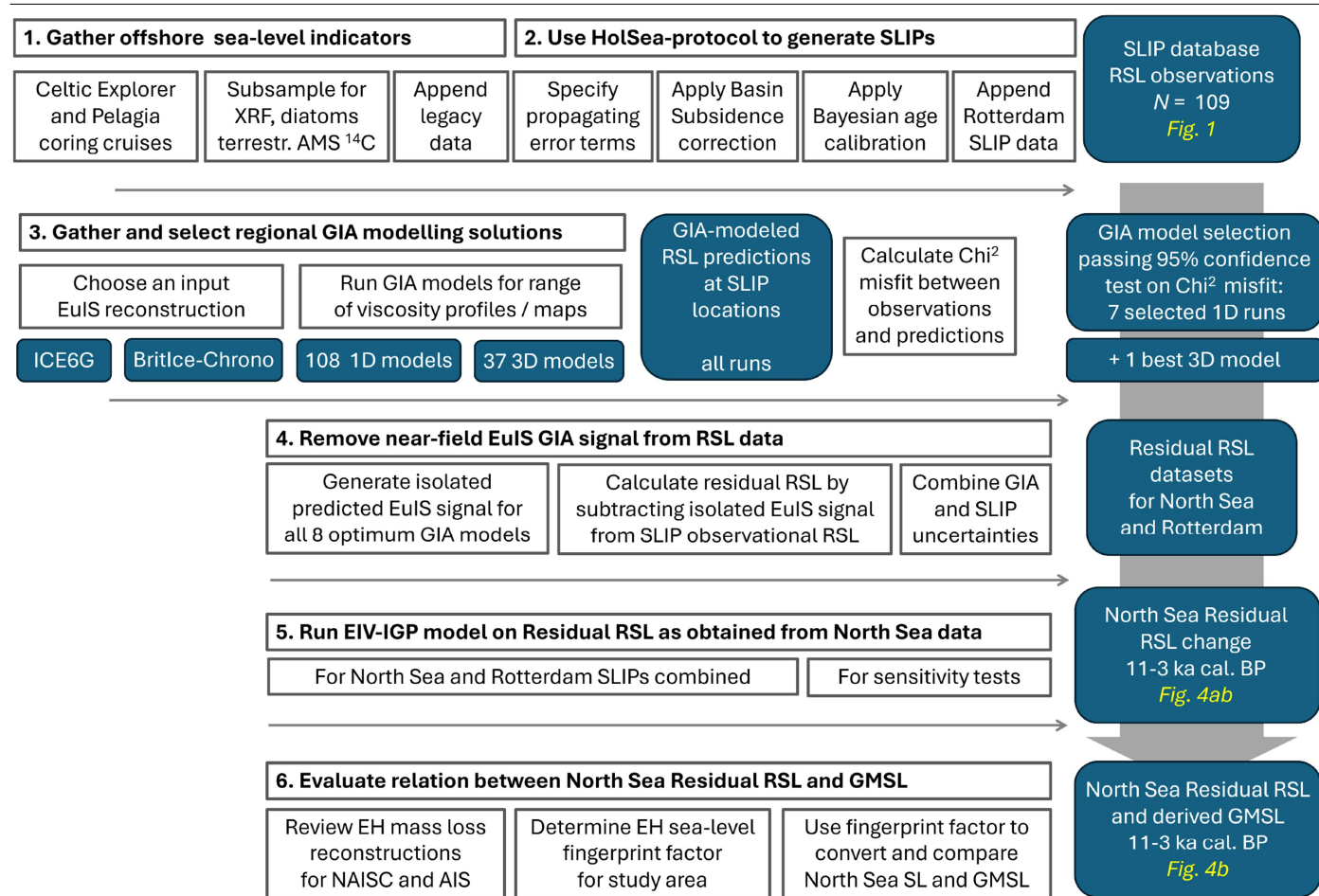
Supplementary information The online version contains supplementary material available at <https://doi.org/10.1038/s41586-025-08769-7>.

Correspondence and requests for materials should be addressed to Marc P. Hijma.

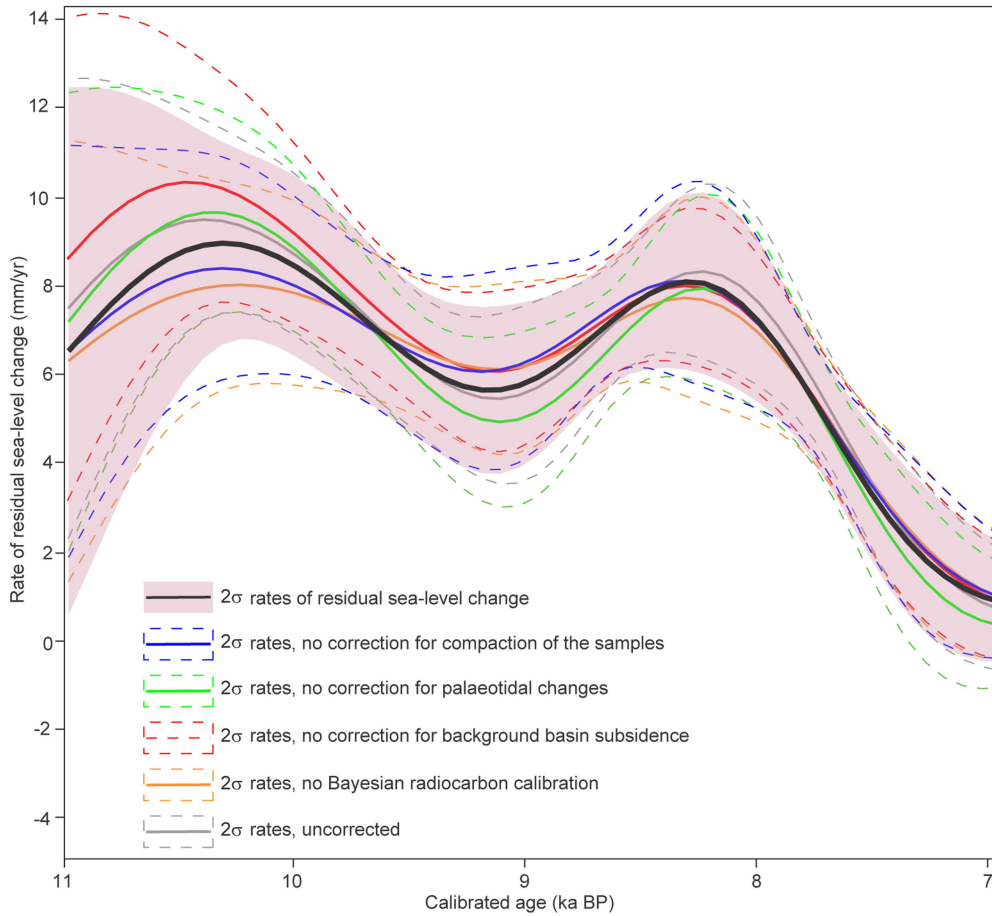
Peer review information Nature thanks Nicole Khan, Andrew Wickert and the other, anonymous, reviewer(s) for their contribution to the peer review of this work. Peer reviewer reports are available.

Reprints and permissions information is available at <http://www.nature.com/reprints>.

Article

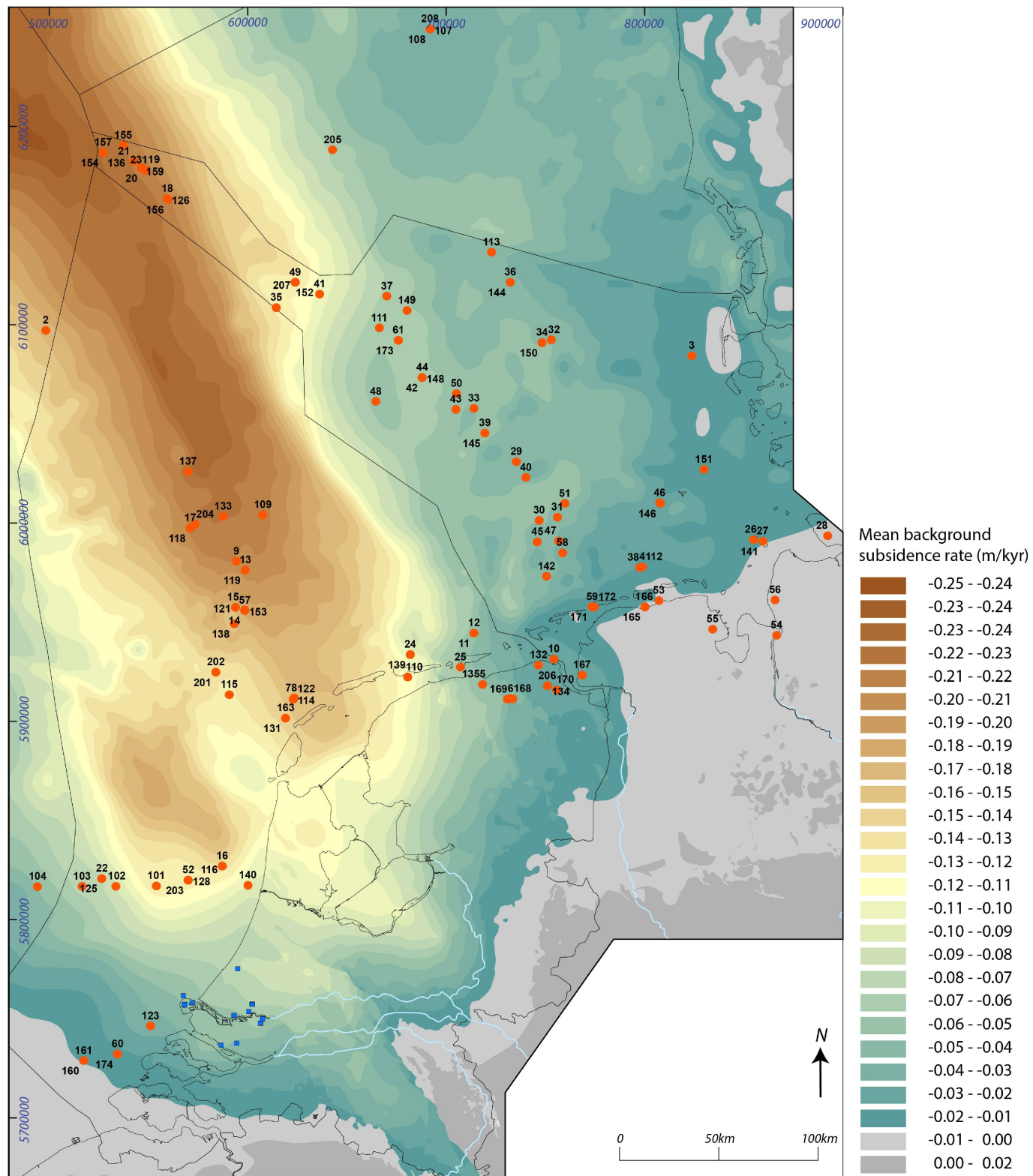


Extended Data Fig. 1 | Overview of the used research workflow to quantify early Holocene GMSL rise. Six steps are defined and cross-referenced in the Methods section.



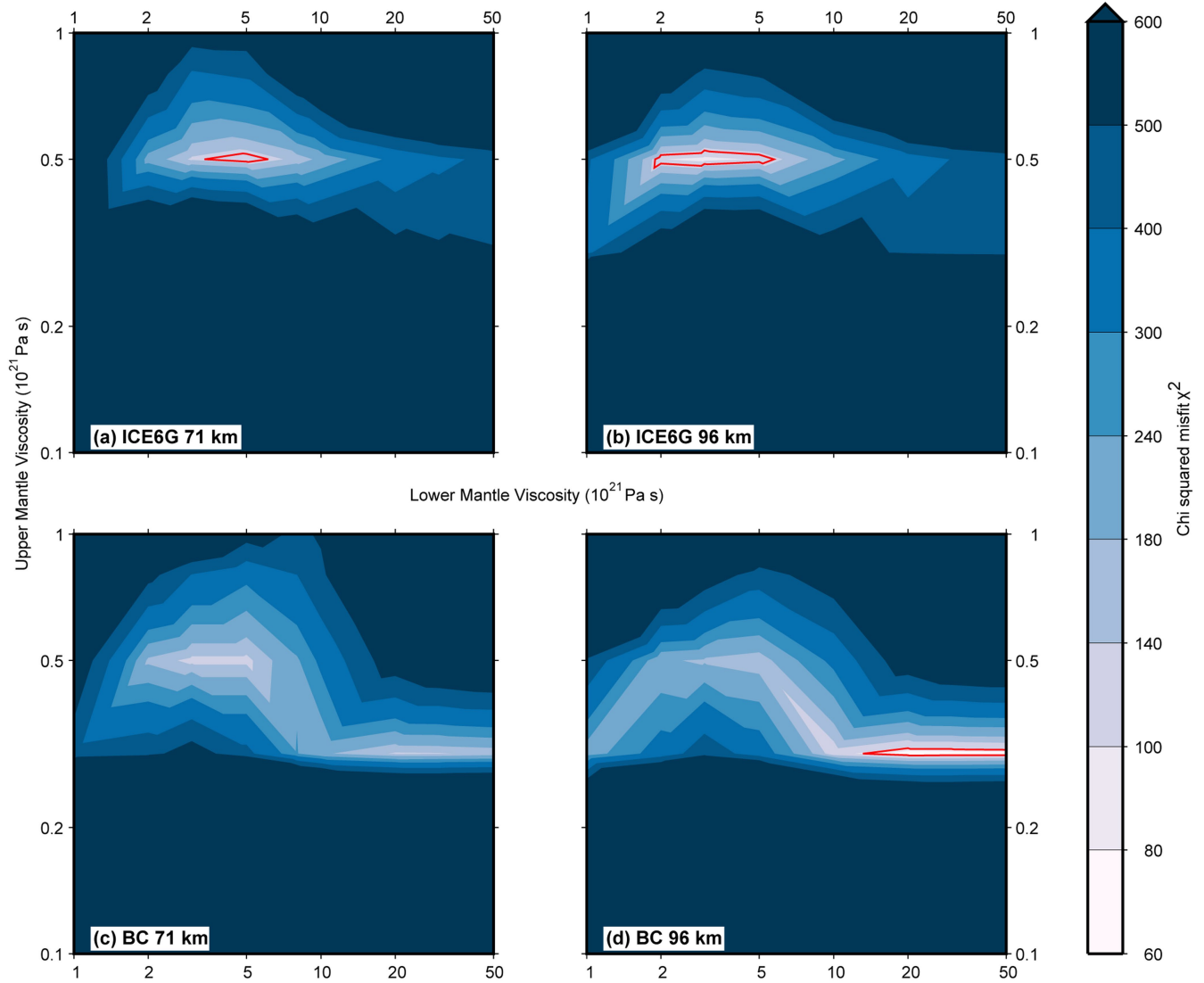
Extended Data Fig. 2 | Sensitivity analysis of the applied corrections. The vertical position and uncertainty of each SLIP was calculated using correction steps for background subsidence, palaeotidal changes and compaction. Calculation of calibrated age and uncertainty (horizontal axis) included a

Bayesian step. The curves and dashed envelopes show the rates when excluding one or all of the steps, besides the all-inclusive run (black line, pink envelope; as in main text). Each correction step has impact, but even without any correction the double peak in the rates remains.

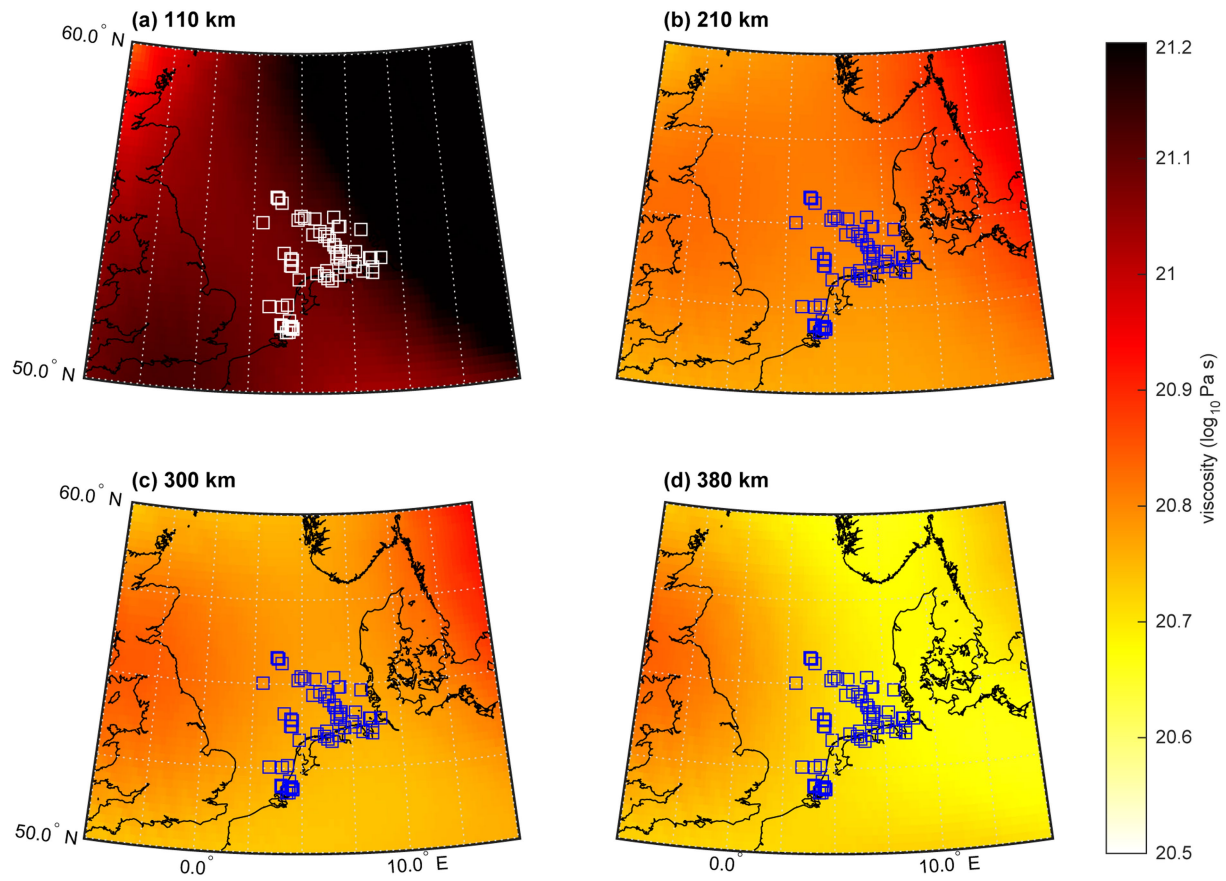


Extended Data Fig. 3 | Mean background subsidence rate (m/kyr) over the last 1.8 Ma for the North Sea Basin. The subsidence rates and associated spatial pattern are not related to GIA processes. Instead, they are a cumulative

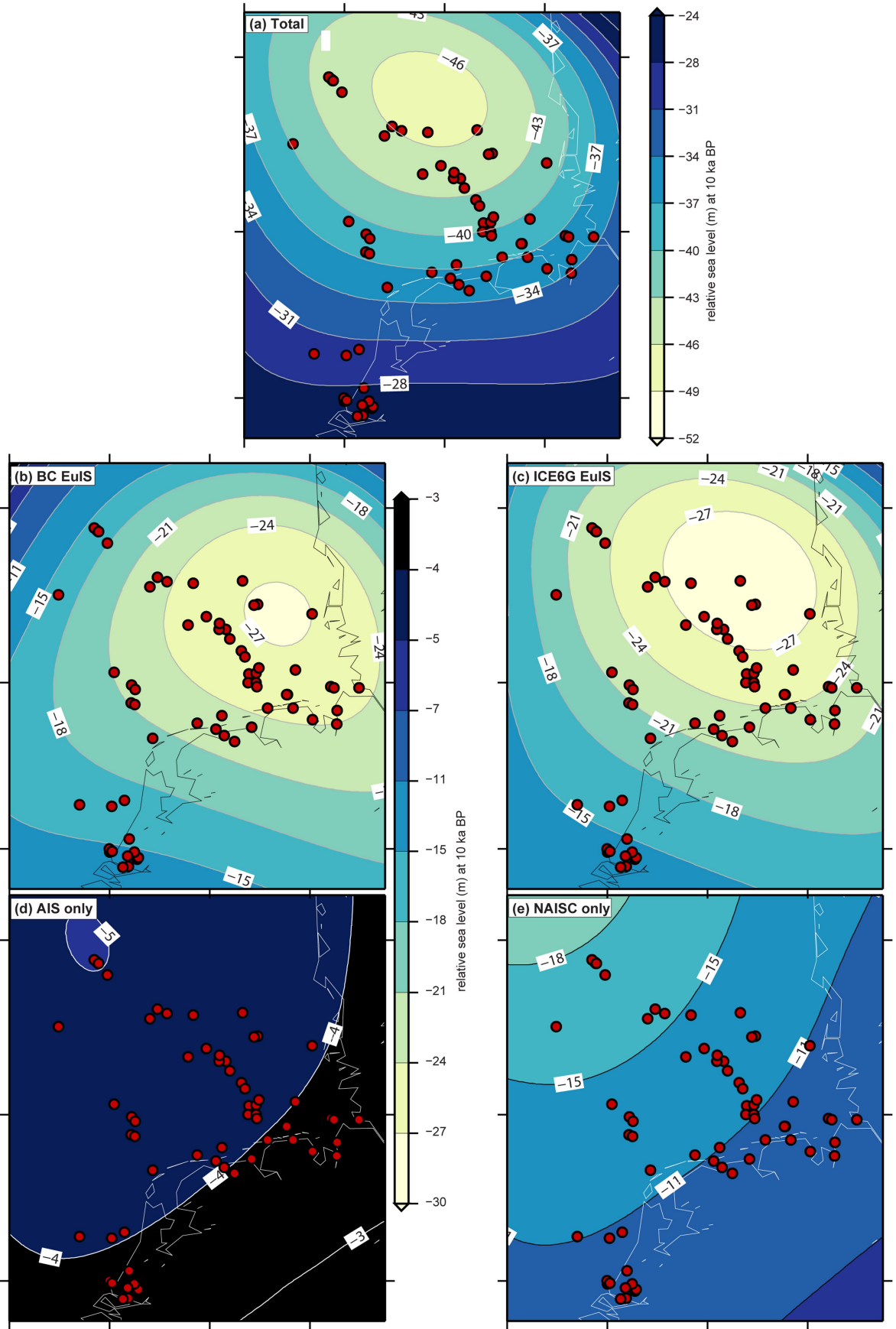
result of tectonics, compaction and sediment loading. Numbered red dots refer to sample identifiers in the database of sea-level indicators (SI Section 1). Blue squares denote the supplemented Rotterdam data cluster.



Extended Data Fig. 4 | Chi-squared (χ^2) misfit values calculated between the predicted and observed sea levels. This was done for a range of upper and lower mantle viscosities and a lithosphere thickness of 71 km (a and c) and 96 km (b and d). The solid red line is the 95% confidence interval calculated for all ICE6G (a and b) and BC (c and d) models. There is no 95% confidence limit on BC with a 71 km lithosphere (c) as all misfits were outside the confidence range.

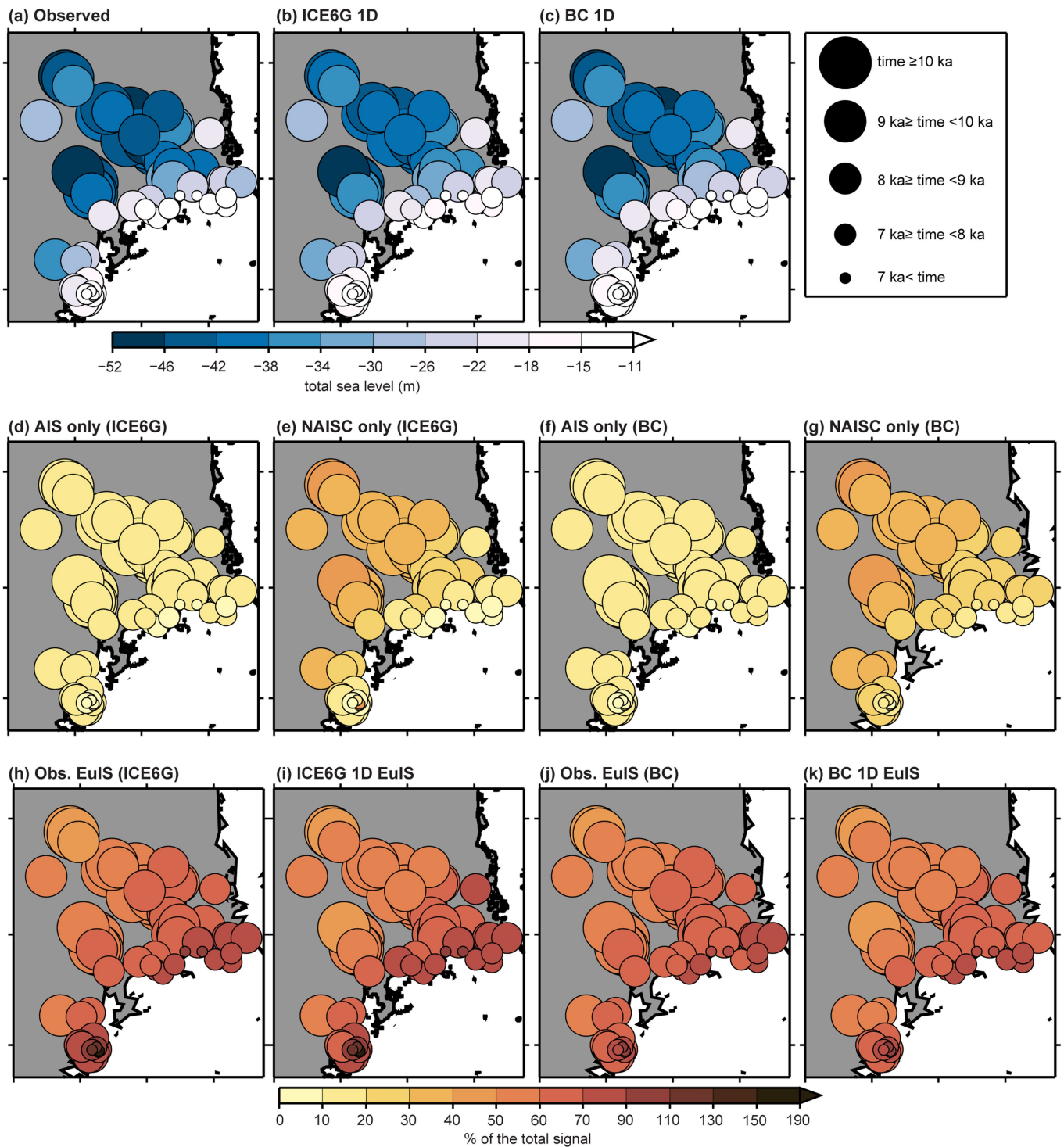


Extended Data Fig. 5 | Viscosity plots for the wider North Sea region. They display viscosity at four depths (a-d), as used in the 3D GIA model SM9925. The figure illustrates the spatial variation of the viscosity profile. The squares (white in panel a, blue in panels b-d) denote the SLIP data sites used in this study.



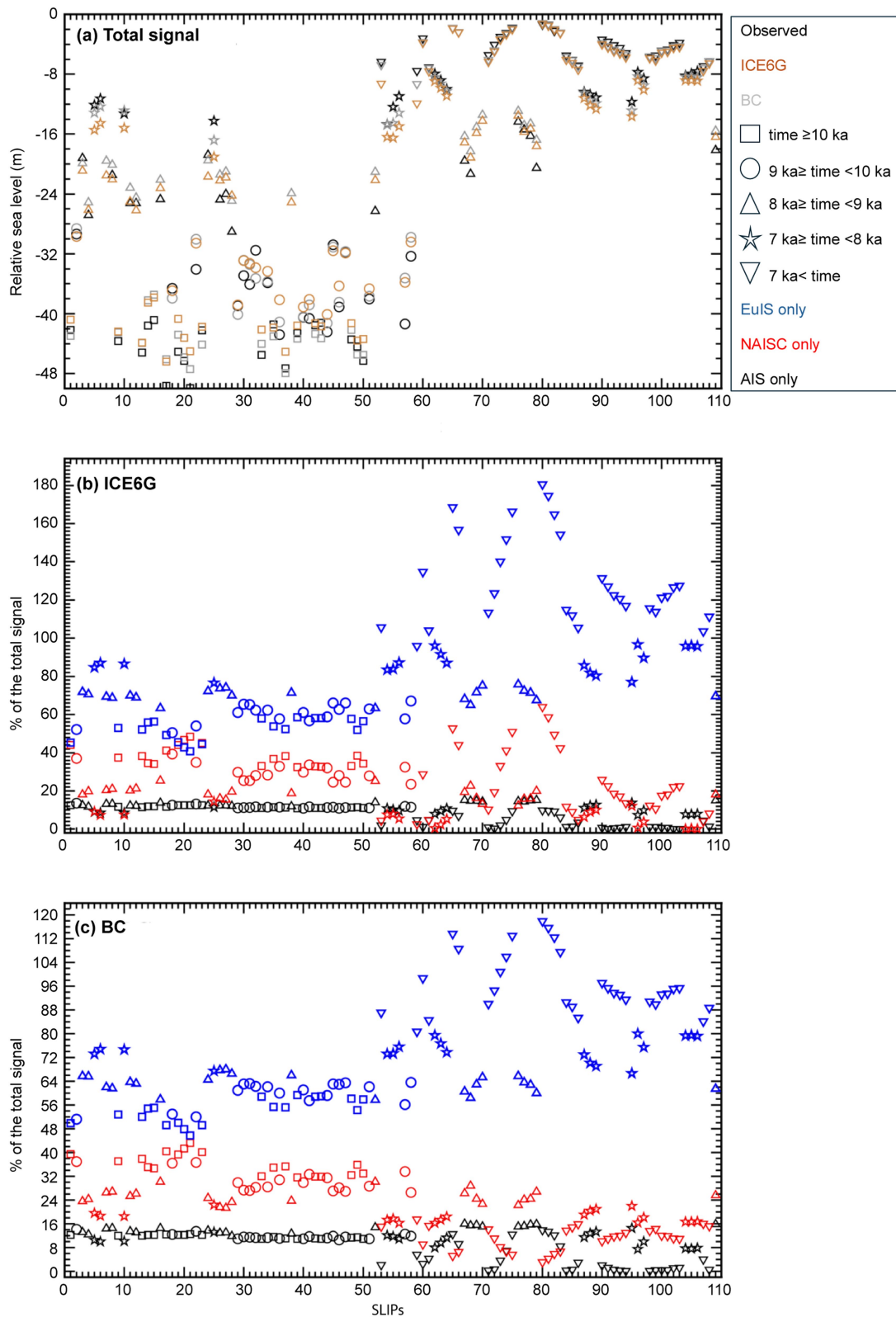
Extended Data Fig. 6 | Predictions of relative sea level at 10 ka from the 1D GIA model using the ICE6G ice-sheet reconstruction¹⁰. The model has a 96 km lithosphere and an upper- and lower-mantle viscosity of 0.5×10^{21} and 3×10^{21} Pa·s respectively, similar to a VM5a earth model. Total signal (a) is the

result for all ice sheets. Further panels separate this into contributions from the Eurasian Ice Sheet (EuS) for the two reconstructions we investigated (b) BC EuS¹⁴ and (c) ICE6G EuS⁹⁴; from (d) the Antarctic Ice Sheet, and from (e) the North American Ice Sheet Complex (including Greenland).



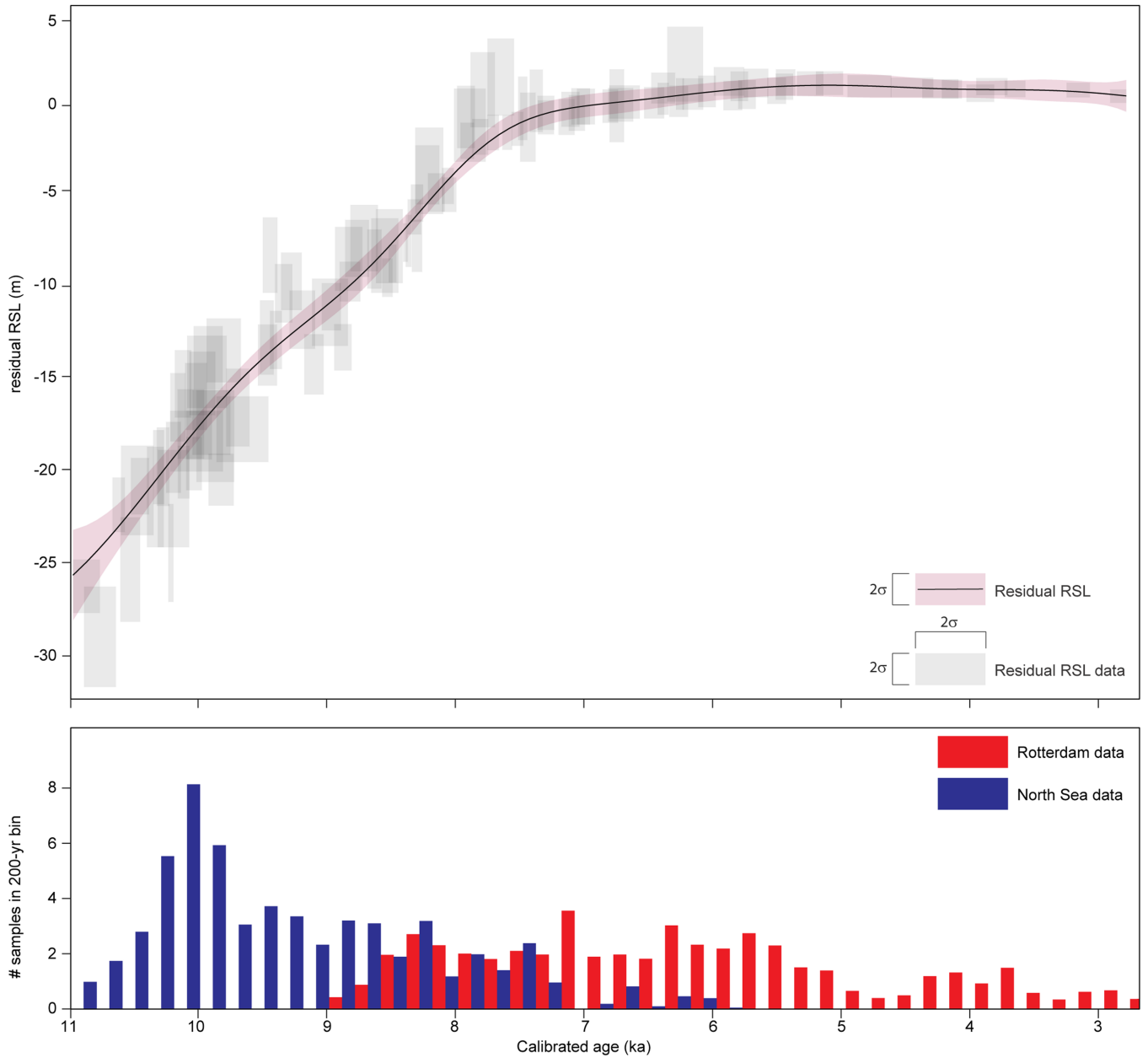
Extended Data Fig. 7 | Observed and predicted relative sea levels (m) for each SLIP location. The observed levels (panel a) include the EuS-signal. Predicted results are shown for 1D ICE6G (b, d, e, h, i) and BC (c, f, g, j, k). Panels d, e, f, g show the signals of the Antarctic (AIS) and North American ice-sheet complexes (NAISC) (from the ICE6G reconstruction) expressed as % of the total

signal using the earth model which produced the lowest misfit, as listed in Extended Data Table 1. Observed (h, j) and predicted (i, k) signals of the Eurasian Ice Sheet (EuS), expressed as % of the total signal, calculated using equations 3 and 4 respectively.

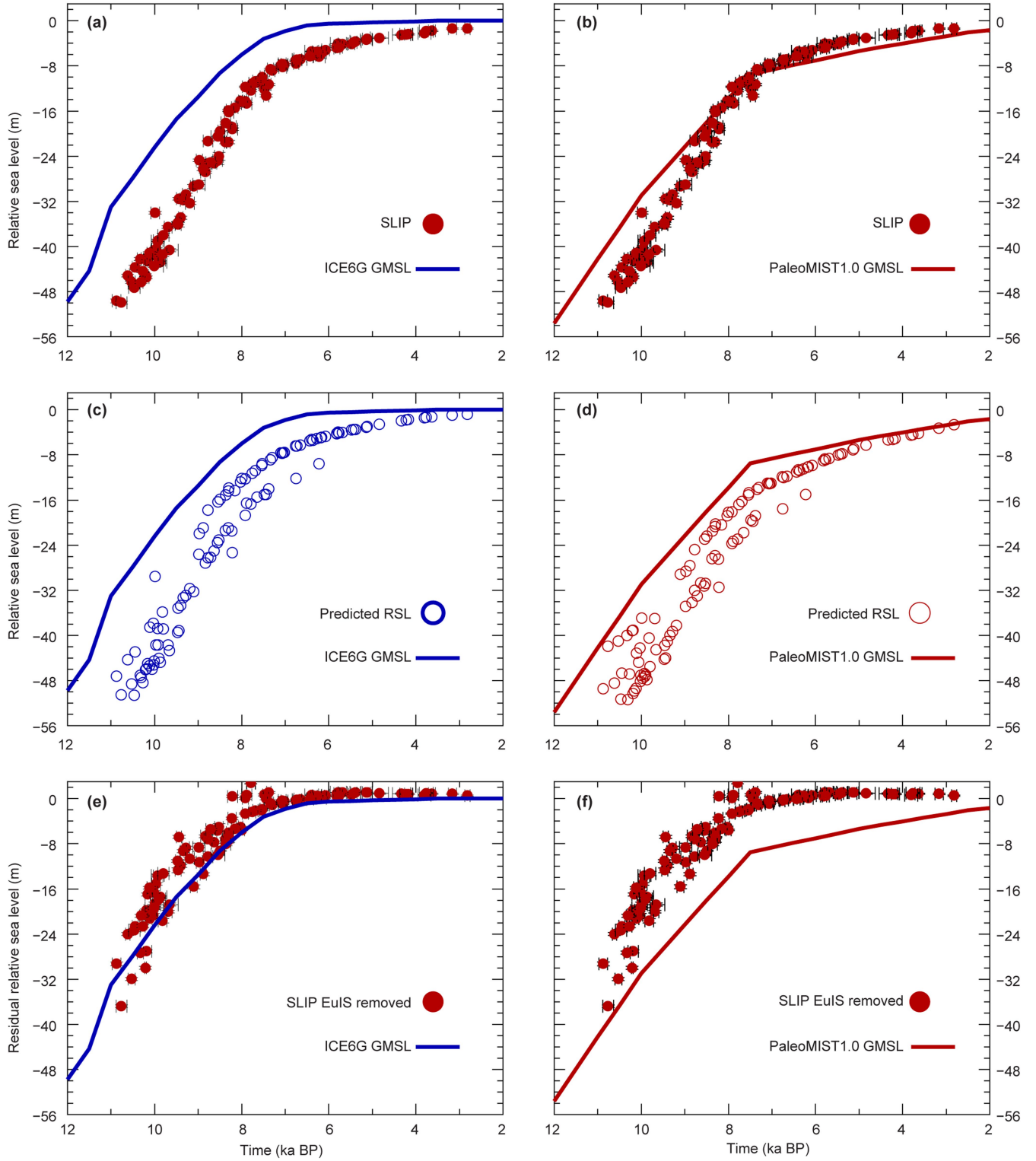


Extended Data Fig. 8 | Observed and predicted sea levels for the two 1D GIA models. In panel a the observations are shown in black, the models in brown (ICE6G) and grey (BC). Panels b (ICE6G) and c (BC) show the contributions from the Antarctic Ice Sheet (AIS, black), North American Ice Sheet Complex (NAISC, red) and the Eurasian ice sheet (EuS, blue) only. Note that at times younger than

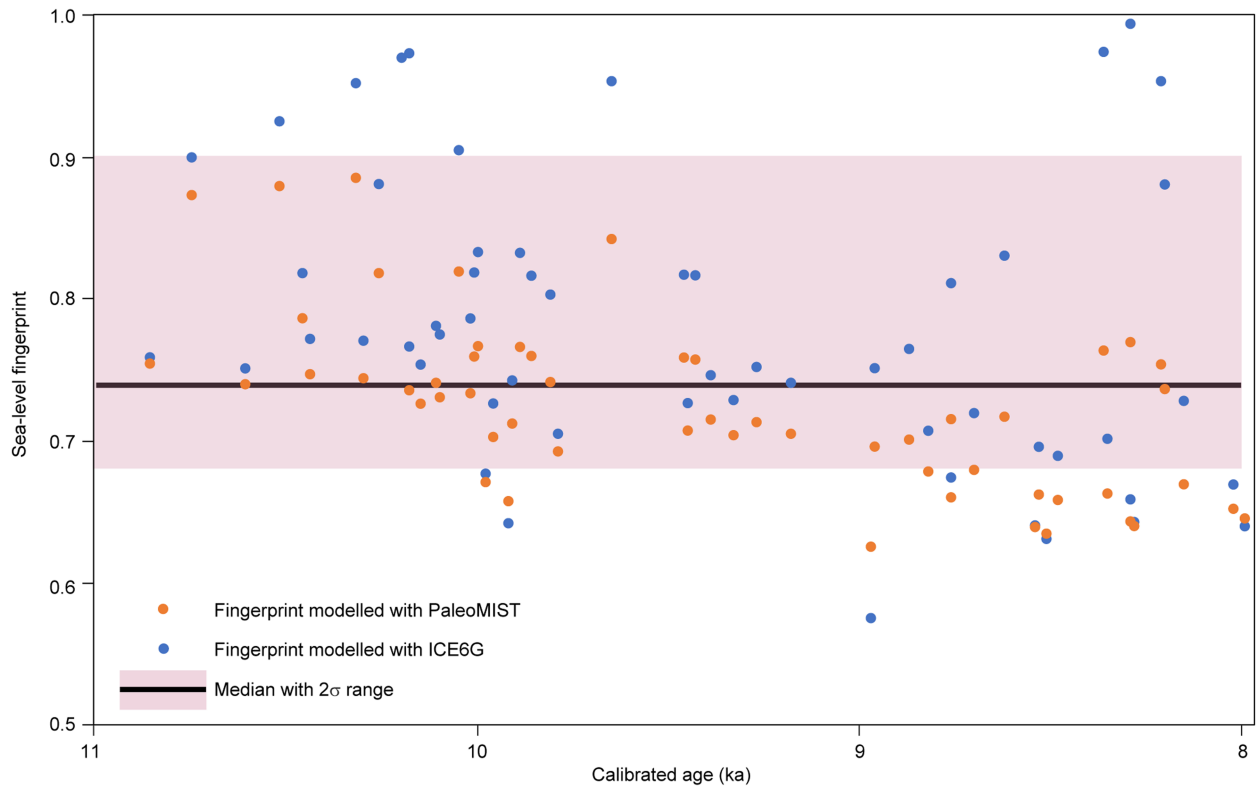
7 ka (inverted triangles) the contribution of the EuS only (blue) is predicted to be more than 100% of the total observed signal. At these times the Predicted EuS RSL contribution is lower than the observed, which results in the values higher than 100%.



Extended Data Fig. 9 | North Sea residual RSL for 11-3 ka. The upper panel shows the residual RSL-curve together with the residual RSL-data. The lower panel gives the number of residual data points per 200-yr bins for the two datasets.



Extended Data Fig. 10 | Differences between published GMSL-curves and RSL data. ICE6G¹⁰ is the blue solid line, PaleoMIST⁸⁹ the red solid line. Results for the observed (geological) RSL data are shown in panels a,b; for the predicted RSL data (all ice sheets) in panels c,d and for the residual RSL data in panels e,f.



Extended Data Fig. 11 | Early Holocene fingerprints. They are derived from ICE6G¹⁰ and PaleoMIST 1.0⁸⁹ output for all individual SLIP locations. Median value is 0.74 (i.e. 74% of modelled GMSL is expected to be recorded in North Sea region in the early Holocene), 2σ range is 0.68–0.90.

Extended Data Table 1 | Chi-squared misfit (equation 1) results for the seven 1D and one 3D GIA models

Ice-sheet reconstruction	Lithosphere thickness (km)	Upper-mantle viscosity (10^{21} Pa·s)	Lower-mantle viscosity (10^{21} Pa·s)	Misfit (m)
1D models				
ICE6G	96	0.5	3	87.34
F test value (95%) = 126	96	0.5	2	101.31
	96	0.5	5	103.99
	71	0.5	5	106.44
BC				
	96	0.3	20	64.69
F test value (95%) = 93.8	96	0.3	30	65.37
	96	0.3	50	69.36
3D model				
ICE6G		SMEAN = beta=0.25		159.64

The misfit results for the full range of 1D viscosity profiles investigated (108 in total) are shown in Extended Data Fig. 4. We investigated two lithosphere thickness (71 km and 96 km) combined with upper and lower mantle viscosities in the range of 0.1 and 1×10^{21} Pa·s and 1 and 50×10^{21} Pa·s respectively. The F test value is a 95% confidence limit used to delimit a misfit region within which the best fit models lie (i.e. misfit values must be below or equal to the 95% confidence limit).